Thermoelastic properties of deuterated melamine, $C_3N_6D_6$, between 4.2–320 K at 5 kPa and between 0.1–5.0 GPa at 295 K from neutron powder diffraction and DFT calculations

A. D. Fortes, N. P. Funnel and C. L. Bull

Thermoelastic properties of deuterated melamine, $C_3N_6D_6$, between 4.2 – 320 K at 5 kPa and between 0.1 – 5.0 GPa at 295 K from neutron powder diffraction and DFT calculations.

A. D. Fortes,[1*] N. P. Funnel,[1] and C. L. Bull[1]

[1]ISIS Neutron Spallation Souce, Rutherford Appleton Laboratory, Harwell Science and Innovation Campus, Chilton, Oxfordshire OX11 0QX, U. K.

Corresponding author: dominic.fortes@stfc.ac.uk

Abstract

We have determined the lattice parameters of perdeuterated melamine, $C_3N_6D_6$, as a function of temperature (4.2 – 320 K) close to atmospheric pressure and as a function of pressure (0 – 5 GPa) at room temperature, using time-of-flight neutron powder diffraction methods. Our observations confirm that the ambient-pressure $P2_1/a$ structure persists throughout this range of P and T. Both the thermal expansion and the compressibility are highly anisotropic; the principal directions of greatest thermal expansion and greatest compressibility are roughly perpendicular to the corrugated sheets of H-bonded melamine molecules that form the main structural motif. Complementary *ab initio* calculations (van der Waals corrected Density Functional Theory) provide an estimate of how the inter- and intra-molecular geometry may alter as a function pressure in the athermal limit.

Keywords: melamine, high-pressure, thermal expansion, compressibility, neutron diffraction

1. Introduction

Melamine ($C_3N_6H_6$, 2,4,6-triamino-1,3,5-triazine) is a simple molecule based on a flat six-sided C–N ring with co-planar amino functional groups attached to each carbon. It is widespread and useful in a variety of biological and industrial processes, being best known as a modern 'plastic' or as an adhesive when mixed with formaldehyde and/or urea to form a resin. The arrangement of H-bond donor/acceptors in the solid crystalline material makes melamine an important tecton for supramolecular synthesis, allowing it to form a broad range of interesting and useful co-crystals [1–3]; probably best known among these is the co-crystal with cyanuric acid which shares a similar pattern of connectivity to that observed in DNA base pairs [4].

The crystal structure of melamine at room temperature was determined by Hughes [5], being monoclinic (space-group $P2_1/a$). The structure has been refined on a number of occasions since then using both X-rays [6–8] and neutrons [9, 10]. The planar melamine molecule forms corrugated sheets lying parallel to the (*201*) plane (Figure 1): four of the six hydrogen atoms form hydrogen bonds with neighbouring molecules in the same sheet; two hydrogen atoms (H3 and H6) form no hydrogen bond at all and simply 'dangle'; atom H5 forms a hydrogen bond out of the plane of the sheet to a melamine molecule in an adjacent sheet (Figure 2). The corrugation of the (*201*) sheets has a wave-vector parallel with *b*, being flat in the orthogonal direction. The sheets have a fabric consisting of 'ribbons' running along the *b*-axis, in which melamine molecules may be viewed as decorating a zig-zag chain of hydrogen-bonded rings. In graph-set terminology [11] these rings are described by the notation $R_2^2(8)$. The ribbons are 'zipped' together with $R_2^2(8)$ rings that run alternately in- and out-of-plane. Clearly, the molecular connectivity in melamine is highly directional and we would expect the physical properties to exhibit a high degree of anisotropy.

Figure 1 and Figure 2 here

There is, similarly, a marked tendency for melamine co-crystals to adopt 2D structures, often forming microporous 2D sheets rather than the densely-packed herringbone arrangement commonly found in cyclic organic molecular crystals [12].

Haussühl [13] reported values for the thermal expansion coefficients, α_i, and elastic constants, c_{ij}, of melamine, confirming the anticipated anisotropy. These values were limited

to a reference temperature of 293 K. Hence the temperature dependence of the thermal expansion and the pressure dependence of the elastic properties remain to be determined.

Due to the interest in melamine as a potential precursor to superhard C–N compounds [14], or N-doped carbon nanotubes [15], a number of studies have been made to characterise its high-pressure behaviour. The earliest of these [16], performed with energy-dispersive X-ray diffraction (EDXRD) on samples contained in a diamond-anvil cell (DAC), observed what was interpreted as a phase transition from the ambient-pressure monoclinic phase to a triclinic phase at 1.3 GPa and then to an orthorhombic phase at 8.2 GPa. However, these conclusions are questionable considering the apparent resolution and level of noise in the diffraction patterns. Given that the proposed powder-pattern indexing also leads to a change in the zero-pressure bulk modulus, K_0, from ~5 GPa to ~55 GPa at the 1.3 GPa transition (when the Reuss bound on the bulk modulus computed from the elastic constants is ~ 11.5 GPa), then there is further scope for doubt in their interpretation.

Subsequent work has proven contradictory: Raman spectroscopy by Liu *et al*. [17] and Odake *et al*. [18] saw no evidence of a phase transition up to 60 GPa; X-ray spectroscopy and X-ray diffraction done by Pravica *et al*. [19] supported the notion that there are two phase transitions in melamine below 24 GPa. In a subsequent EDXRD study, Pravica *et al*. [20] made measurements principally at high P <u>and</u> high T, but did collect data at 3.5 GPa at room temperature, which they asserted could be indexed with the same $P\bar{1}$ cell reported by Ma *et al*. [16]. Galley *et al*. [21] made the most definitive XRD study to date, interpreting their data in terms of phase transitions at 2, 8 and 16 GPa. Again, these interpretations appear to rest on quite subtle peak splitting, or the disappearance of shoulders and/or isolated very small peaks. Given the highly anisotropic elastic properties of melamine [13] and the large pressure increments typically used in the aforementioned DAC studies, we consider it plausible that these so-called phase transitions simply reflect anisotropic peak shifts; Bragg peaks positions that are determined most strongly by soft directions in the crystal will inevitably shift substantially under compression, merging with or passing through Bragg peaks with Miller indices corresponding to stiffer directions in the crystal.

The objective of this work is principally to establish, by means of high-pressure neutron powder diffraction, whether these high-pressure phase transformations do indeed occur, and to accurately determine the pressure dependence of the lattice parameters. Furthermore, we aim to determine the thermal expansion tensor as a function of temperature and to present complementary *ab initio* calculations.

Subsequent to our data collection and during the preparation of this manuscript, a high-pressure single-crystal X-ray diffraction study was published by Shelton *et al.* [22], confirming our suspicions with regard to the absence of phase transitions below 30 GPa. We communicate detailed comparisons between our results and those of Shelton *et al.* [22] below.

2. Experimental Method

2.1 Deuteration

Perdeuterated melamine was prepared by recrystallization of 'ordinary' protiated material (Aldrich M2659, 99 %) from D_2O (Aldrich 151882, 99.9 atom % D) followed by equilibration of the partially deuterated material in boiling D_2O for several hours. Raman spectra of the as-purchased H-analogue and the product of equilibration in hot D_2O were collected using a B&WTek *i*-Raman Plus spectrometer (40 mW, 532 nm) to confirm the almost complete deuteration (Supplementary Figure S1).

2.2 Variable-temperature neutron powder diffraction

6.8 g of melamine-d6 was loaded into a slab-geometry holder composed of Al-alloy 6082–T6, with interior dimensions of 18 x 23 mm perpendicular to the incident-beam direction and a depth of 15 mm parallel with the neutron beam. These holders have holes drilled either side of the specimen, one to accept a RhFe resistance thermometer, fully calibrated on the ITS-1990 scale, and the other to take a cartridge heater (Watlow Firerod C1E-192). The open front and back faces of the holder are covered with 125 μm-thick vanadium foil windows, sealed in place with steel frames and indium wire. Exposed steel and Al surfaces on the front of the sample holder are masked from the incident beam with Gd and Cd foils.

The slab-can was mounted on the end of a cryostat centre stick and inserted into a 50 mm-bore 'Orange' He cryostat. The temperature of the sample was then reduced to 4.2 K for the initial data collection. Although the windows of the sample can are sealed with indium wire, it is not possible to determine if the joints are hermetically sealed; it is likely, therefore,

that the interior space is under the same pressure of helium gas as the surrounding heat-exchange space, this being in the region of 50 mbar.

Neutron powder diffraction data [23] were collected on the High Resolution Powder Diffractometer (HRPD) at the ISIS neutron spallation source, Oxfordshire, U.K. [24, 25]. In its standard configuration, data were initially collected in a 100 ms-wide time of flight window, covering the range from 30 – 130 ms (incident beam jaws' gap set at 15 x 20 mm w x h), measuring for ~ 3 hr, equivalent to 120 μA of proton-beam current. The instrument's chopper phasing was then altered to collect data in a time-of-flight window spanning 100 – 200 ms. The advantage of this window is that it brings Bragg peaks with d-spacings from 2.2 – 4.0 Å into 'view' of the instrument's highest-resolution backscattering banks. For many materials, the strongest Bragg peaks are in this d-spacing range such that, despite the lower incident flux across the 100 – 200 ms time window, it is often possible to collect data with good statistics suitable for lattice-parameter refinement more quickly than in the 30 – 130 ms window. At 4.2 K, a further 3 hr data collection was made in the 100 – 200 ms window, and all subsequent data were acquired, in 10 K increments on warming, with the same instrument configuration.

Warming was achieved by applying power to the *in situ* cartridge heater, taking care to maintain a slow-ramp of 3 K min^{-1} on moving from one temperature to the next and waiting for 10 minutes once the measured temperature of the sample holder was within ± 2 K of the requested set-point. In the absence of a sample-embedded thermometer, off-line testing reported elsewhere [26, 27] has shown that this strategy ensures proper equilibration of low thermal conductivity powder specimens such that the measured frame temperature is an accurate determination of the true sample temperature.

It later became apparent that a very small region of negative linear expansion might be present along the crystal's *b*-axis below ~ 30 K. In order to confirm this, a further set of data were collected, using the same batch of material and the same sample holder as before, but with cooling provided by means of a closed-cycle refrigerator (CCR) with a Sumitomo RDK-415D cold head. These data were measured in HRPD's 30 – 130 ms time-of-flight window in 5 K increments on warming from 10 – 75 K; two additional points were measured at 100 and 200 K.

Finally, a reference dataset was measured at 297 K from melamine-d6 powder loaded into a standard 8 mm diameter vanadium can. The purpose of this was to try and obtain a

diffraction pattern free of the substantial preferred orientation seen in the two slab-geometry samples and free of the background from the cryostat or CCR.

Data measured in each detector bank were focused to a common scattering angle, normalised to the incident spectrum and corrected for detector efficiency by reference to a V:Nb standard using the Mantid library of diffraction algorithms [28, 29].

2.3 Variable-pressure neutron powder diffraction

Room-temperature high-pressure measurements on melamine-d6 [30] were carried out on the PEARL beamline at the ISIS neutron spallation source, Oxfordshire, U.K. [31] using an oil-driven V3 variant Paris-Edinburgh (P-E) opposed-anvil press. The powder sample was loaded into encapsulated TiZr gaskets [32], along with an *in-situ* pressure calibration standard consisting of a 50 mg ball of compacted Pb foil; the mixture was wetted with a 4:1 mixture of perdeuterated methanol:ethanol and sealed closed under an applied load of 6 tonnes with zirconia-toughened alumina (ZTA) anvils.

Data were collected in the instrument's 90° detector banks, with a time-of-flight window extending from 1.5 – 20 ms, covering a d-spacing range from 0.3 – 4.1 Å. Measurements were made in load increments of 2 tonnes up to 32 tonnes and increments of 2.5 tonnes from 35 – 60 tonnes.[1] Counting times were 3 hr each up to 24 t, being extended to 4 hr subsequently to offset the effect of a reduced gap between the anvils through which the diffracted beam is detected; the final measurement at 60 t ran for 6 hr. The internal pressure, determined from the equation of state of the enclosed Pb standard [33], increased at the expected rate of ~ 0.1 GPa per tonne. An anomaly in the load-curve was noted at 45 t; after investigation, measurements were resumed from a load of 52 t with a noticeable broadening of the Bragg peaks and (as will be shown later) substantial deviations from the fitted equations of state. However, no evidence of a phase transformation could be observed in the diffraction data and no unambiguous sign of a gasket failure was visible so the origin of the anomaly is not known.

Upon completion of the final measurement at 60 tonnes, the sample was decompressed, removed from the press (remaining inside the TiZr gaskets) and measured one week later on PEARL under zero load at room temperature for 1.7 hr.

---

[1] The exact relationship between load and pressure is given in Supplementary Table S2.

Time focussing, normalisation to the incident spectrum, corrections for instrument efficiency and corrections for the attenuation of the anvils were all carried out using Mantid powder diffraction routines [28, 29]. An example stack-plot of the powder diffraction data obtained on PEARL is shown in Figure 3 by way of comparison with some of the earlier synchrotron X-ray diffraction data.

Figure 3

2.4 Density-Functional Theory Calculations

In order to aid in the interpretation of some of our experimental data we carried out a series of first-principles calculations using Density Functional Theory, DFT, and the plane-wave pseudopotential method [34, 35]. The calculations were carried out using CASTEP [36–38] in conjunction with the analysis tools in the Materials Studio software package. Tests for convergence of the total energy and of structural parameters were done by varying the basis-set cut-offs and the reciprocal-space sampling. Calculations were done using the PBE generalized-gradient approximation functional [39] and Tkatchenko-Scheffler van der Waals dispersion corrections [40] with ultrasoft pseudopotentials; a basis-set cut-off of 1000 eV and a $3{\times}3{\times}4$ $\vec{k}$-point grid ($\sim$ 0.04 Å^{-1} reciprocal lattice spacing) achieved a satisfactory convergence of the total energy as well as excellent agreement with the structure determined at 14 K [10].

Geometry optimizations were carried out at a series of fixed hydrostatic pressures from -1 to $+20$ GPa in which both the ions and the unit-cell were allowed to relax.

3. Results

Whole-pattern profile refinement of the neutron powder diffraction data was carried out in GSAS/Expgui [41, 42]. Each pattern was fitted initially by the Rietveld method [43], varying lattice parameters, background coefficients, scale factors, peak-profile coefficients and isotropic displacement parameters. The final refinement of the lattice parameters was done using the "F(calc) weighted" method in GSAS, which employs the Rietveld model as its starting point in order to fit each Bragg peak more accurately; this relative of the LeBail method [44] typically yields the highest lattice-parameter precision. All of our specimens exhibited a substantial degree

of preferred orientation, in particular the well-packed slab-geometry samples used in the variable-temperature study. The choice of model-independent profile refinement was thus especially suited to extraction of high-precision lattice parameters. For the well-counted high-pressure datasets, stiff-bond-distance restraints were necessary in order to achieve a stable structure refinement; consequently, only the <u>inter</u>molecular distances and angles are meaningful. Shelton *et al*. [22] were obliged to impose geometric restraints on the hydrogen atoms in their single-crystal refinements; as such, the DFT calculations presented here represent the only accurate information on the evolution of all molecular distances and angles with pressure.

The refined lattice parameters collected on HRPD as a function of temperature are tabulated in Supplementary Table S1 and illustrated in Figure 4 (50 points); those collected on PEARL as a function of pressure appear in Supplementary Table S2 and Figure 5 (23 points); those obtained from the DFT optimizations are given in Supplementary Table S3 (20 points).

Figure 4 and Figure 5

3.1 Thermal expansion

As shown in Figure 4, the lattice parameters all behave normally above 30 K; by contrast, the *b*-axis exhibits an extremely small degree of negative linear expansion below 30 K (See expanded view in Supplementary Figure S2), the magnitude of which is ~ 5 times smaller than the negative linear expansion observed in ice I*h* below 60 K [26]. Table 1 compares the lattice parameters obtained on HRPD at 4.2 K and at 15 K with the athermal zero-pressure DFT result and with the accurate but quite imprecise 14 K lattice parameters of Cousson *et al*. [10].

Table 1

Various physically meaningful functions may be used to fit the temperature dependence of the lattice parameters, including models based on Debye-type and/or Einstein-type approximations of the material's vibrational density of states (VDOS). Since the Debye-type models that we have used to fit the thermal expansion are (*i*) fairly complex to evaluate, (*ii*) provide limited insight into the underlying vibrational modes and (*iii*) are only dimensionally correct for the volume, we present that analysis in the Electronic Supplement and here restrict ourselves to a much simpler and more general – but nevertheless accurate – approach to

fitting the individual lattice parameters. The thermal expansion is described by a linear combination of a power law and an exponential function;

$$X(T) = X_0 + [(p \cdot T^{-q/T}) + (r \cdot e^{-s/T})]/(e^{1/T} - 1) \qquad (1)$$

where p and r are scaling terms and q and s are 'characteristic temperatures' that are indicative of the function's saturation behaviour. This function lacks the oscillatory behaviour of polynomial functions, gives the correct saturation behaviour at low temperature (i.e., $\alpha > 0$ as $T > 0$) and effectively partitions the thermal expansion into two regions: the low-temperature part is driven by the internal energy of the acoustic vibrational modes in the crystal; the higher-temperature part is driven by the internal energy of the optical modes.

As can be seen from Supplementary Figure S3, the difference in volume thermal expansion between this model and the double-Debye model described in the Supplement is quite small and indeed can only be distinguished in the expanded plot of the low-temperature region. The power/exponential model is thus a simple but accurate representation of the thermal expansion despite its *ad-hoc* nature. The model was used to fit each of the unit-cell metrics, fit parameters being given in Table 2. For the *b*-axis, the very small magnitude of the negative thermal expansion and its limited extent in T (meaning only a few measurement points could be used to fit it) made it impossible to obtain an accurate description of this low-temperature region. As a result, the *b*-axis data were only fitted above 30 K and the extent of the misfit below this can be seen clearly in Supplementary Figure S2.

Table 2

Pairs of adjacent experimental lattice parameters were used to calculate a symmetric strain tensor – the thermal expansion tensor with coefficients α_{ij} – and from there to obtain the magnitudes and direction cosines of the principal thermal expansivities, α_i, by standard matrix decomposition methods. Haussühl [13] determined α_{ij} for melamine at 293 K as follows: $\alpha_{11} = 107 \times 10^{-6}$ K^{-1}, $\alpha_{22} = 22 \times 10^{-6}$ K^{-1}, $\alpha_{33} = 29 \times 10^{-6}$ K^{-1}, $\alpha_{13=31} = 38 \times 10^{-6}$ K^{-1}. Our values are in excellent agreement, being (at 293 K), $\alpha_{11} = 105(2) \times 10^{-6}$ K^{-1}, $\alpha_{22} = 18(2) \times 10^{-6}$ K^{-1}, $\alpha_{33} = 28(2) \times 10^{-6}$ K^{-1}, $\alpha_{13=31} = 38(2) \times 10^{-6}$ K^{-1}.

Figure 6

The magnitudes of the volume- and principal linear thermal expansion coefficients as a function of temperature are plotted in Figure 6, along with the values obtained from the Power/Exponential-model fit and those derived from Haussühl's α_{ij}. Individual plots of the α_i, with expanded vertical scales and showing both series of HRPD data are provided in Supplementary Figure S4; these highlight the very small negative α_2 below 30 K. The expansion tensor is fixed by symmetry to have one principal direction (α_2) aligned with the 2-fold axis of the crystal; an intuitive and useful metric to describe the orientation of the other two principal directions is shown at the bottom of Figure 6, where the angle (φ) between α_1 and the normal to the (*201*) plane is plotted. Entirely unsurprisingly, the thermal expansion is very large along the direction in which the corrugated sheets are stacked and very small in the plane of the sheets, the tilt-angle varying by less than 10° over the whole range of temperatures that were measured. The differences in the volume- and the principal linear thermal expansion coefficients between this work and Haussühl [13] at 293 K are just within the uncertainty of our measurements but the systematic positive offset of Haussühl's values could be due to protiated melamine having a marginally greater thermal expansivity than the deuterated analogue at a given temperature.

3.2 Compressibility

The agreement, shown in Figure 5, between the high-pressure unit-cell parameters we obtain and those reported by Shelton *et al*. [22] is excellent. This high degree of reproducibility, considering the differences in experimental methods (and indeed differences in isotopic composition) confirm the impression outlined in the introduction that some of the previous high-pressure studies were misguided in the interpretation of their results.

The data collected on compression along the room-temperature isotherm were fitted, using the program EosFit [45] with a third-order Birch-Murnaghan equation of state [46, 47], which is parameterised in terms of the zero-pressure volume (V_0), zero-pressure isothermal bulk modulus ($K_0 = -V \, \partial P/\partial V$), and the first pressure derivative of the bulk modulus (K'). It should be noted that K″ (the second pressure derivative of K_0), has a finite non-zero value: K″ = (K′/K_0)(7−K′)−(143/24)(8/3K_0). From a fit to the unit-cell volumes, we find V_0 = 536.7(6) Å^3, K_0 = 12.0(5) GPa, K′ = 7.8(5) and an implied K″ = −1.84(8) GPa^{-1}. Shelton *et*

al. [22] fitted a Vinet equation of state to their data but obtained parameters very similar to ours; $V_0 = 536.7(2)$ Å^3, $K_0 = 12.9(8)$ GPa, and $K' = 7.4(3)$.

A similar procedure was used to fit the individual cell dimensions, with parameters listed in Table 3; the monoclinic angle β was treated with a third-order polynomial. Shelton *et al.* [22] list linear compressibilities of the three unit-cell edges (although the means by which these were determined is not stated), from which we derive axial incompressibilities for comparison with values in Table 3 of $K_a = 51.0(4)$ GPa, $K_b = 176(1)$ GPa and $K_c = 37.0(4)$ GPa.

Table 3

Naturally the compressibility, like the thermal expansion, is a tensor quantity with only one principal axis fixed by the monoclinic symmetry of the crystal. A more useful description of the structure's response to hydrostatic pressure, and a means of direct comparison with the measured elastic constants, is thus obtained by calculation of the symmetric strain tensor between adjacent pairs of cell parameters and the determination of principal values and direction cosines by matrix decomposition. The pressure dependence of the ε_{ij} from our experimental data, the Birch-Murnaghan fit and from the DFT calculations is depicted in Figure 7.

Figure 7

The 6×6 elastic stiffness matrix of c_{ij} reported by Haussühl [13] is inverted to obtain the 6×6 elastic compliance matrix of s_{ij}. The coefficients of the elastic strain tensor, ε_{ij}, are then:

$\varepsilon_{11} = s_{11}+s_{12}+s_{13} = 0.0532(5)$ GPa^{-1};

$\varepsilon_{22} = s_{12}+s_{22}+s_{23} = 0.0056(4)$ GPa^{-1};

$\varepsilon_{33} = s_{13}+s_{23}+s_{33} = 0.0284(8)$ GPa^{-1};

$\varepsilon_{12=21} = 0$;

$\varepsilon_{13=31} = s_{15}+s_{25}+s_{35} = 0.0535(14)$ GPa^{-1};

$\varepsilon_{23=32} = 0$.

For the most part, there is good agreement between these ambient-pressure values and the observations reported in Figure 7. The exception is $\varepsilon_{13=31}$, which is off-scale-high on the

bottom-right panel of Figure 7, indicative of one of three possibilities: (1) Our result is correct and Haussühl's resonant ultrasound spectroscopy produced inaccurate values for the off-diagonal terms of the elastic compliance matrix; (2) both our result and Haussühl's c_{ij} are correct and there is a real difference in the elastic properties of H- and D-melamine; (3) Haussühl's values are correct and our determination of $\varepsilon_{13=31}$ at low pressure is wrong. The latter could occur by virtue of the limited low-pressure sampling we can achieve with the Paris-Edinburgh press where $\varepsilon_{13=31}$ might possibly undergo a very rapid stiffening. Determining which of these is correct will necessitate re-measuring the elastic constants of protiated melamine, measuring the elastic constants of deuterated melamine and perhaps also carrying out a high-pressure neutron diffraction study of melamine-d6 in the range $0 < P <$ 500 MPa using, for example, a gas-pressure cell.

The values given in Figure 7 are transformed into their principal magnitudes by matrix decomposition and plotted as their inverse quantities (i.e., as linear incompressibilities, K_i) in Supplementary Figure S5. The effect of the large difference in $\varepsilon_{13=31}$ is to introduce a disparity in the incompressibility along the principal direction most closely aligned with the c-axis, K_3, where Haussühl's c_{ij} actually lead to a negative linear incompressibility. It is difficult to accept, examining our experimental and computational values of K_3, that statement number (3) in the preceding paragraph is a viable possibility. As with the thermal expansion tensor, the direction of greatest compressibility (smallest incompressibility) is nearly perpendicular to the (*201*) plane; the angle φ between K_1 and the normal to (*201*) varies from −5° to −10°, the negative value denoting that the vector is tilted towards the *c*-axis direction rather than towards *a*. A direct visual comparison between the representation surfaces of the thermal expansion tensor and the compressibility tensor, and their orientation with respect to the unit-cell edges and the (*201*) plane appears in Figure 8.

Figure 8

The estimated zero-pressure linear incompressibilities and their first pressure derivatives are: K_1 = 15.4(5) GPa, K_1' = 11(1); K_2 = 156(3) GPa, K_2' = 41(3); K_3 = 85(2), K_3' = 30(2). The Reuss bound on the bulk modulus, K_R, which is the appropriate value to compare with the bulk modulus obtained from a series of measurements made under hydrostatic compression is defined as $[(s_{11}+s_{22}+s_{33}) + 2(s_{12}+s_{13}+s_{23})]^{-1}$; using Haussühl's c_{ij} leads to a

value of 11.5(1) GPa, which is not statistically different from our zero-pressure bulk modulus of 12.0(5) GPa.

Considering that these *ab initio* calculations were done in the athermal limit, such that the DFT zero-pressure unit-cell volume differs by 5.0 % from V_0 in our room-temperature Birch-Murnaghan equation of state, it is to be expected that the calculated elastic properties will be stiffer than observed experimentally. Nevertheless, a calculated zero-pressure, zero-temperature bulk modulus of 17 GPa only requires $dK/dT \approx -0.016$ GPa K^{-1} in order to be consistent with the experimental measurements, which is a perfectly reasonable value similar to what is observed in other hydrogen-bonded solids, -0.01 to -0.03 GPa K^{-1} [48–52].

A direct comparison of our experimental and computational equations of state with the experimental results of Ma *et al.* [16] and Shelton *et al.* [22] is given in Supplementary Figure S6.

4. Structural changes at high pressure

Loose intramolecular bond-distance restraints were necessary to achieve a stable structural refinement of the high-pressure neutron diffraction data; the internal angles remained sensible without imposed restraints, although the values are imprecise and no meaningful pressure-dependence may be discerned. Hence the only unbiased and reasonably precise experimental structural parameters we are able to report are the intermolecular distances and angles. Shelton *et al.* [22] imposed restraints on the H-atom positions, which has the unfortunate effect of flattening the N3 amine group (which should be twisted in such a way as to form the inter-sheet H-bonds) into near co-planarity with the rest of the melamine molecule. The uncertainty they report on C–N bond lengths are, at best, comparable to the pressure-induced shortening of these contacts we find in our DFT calculations (see below) and furthermore exhibit no perceptible pressure dependence.

By contrast, the DFT calculations permit a highly precise determination of the weakly pressure-dependent changes in intramolecular geometry to be appreciated – with the caveat that potentially significant temperature-dependent vibrational contributions are not accounted for. The accuracy of the lattice parameters (as noted in Table 1) is extremely good, and a comparison of the C–N bond lengths at zero-pressure with those found experimentally by Cousson *et al.* [10] is also excellent. The triazine-ring C–N bond lengths are in good absolute agreement, including the spread of distances (0.0166 Å from DFT, 0.016(2) Å from the 14 K single-crystal measurement) and the order: as shown in Figure 10, the length of the triazine

C–N bonds at 0 GPa decreases as C1–N5 > C2–N4 > C2–N6 > C1–N1 > C3–N5 > C3–N4 and this differs from the experimentally-observed order only in respect of the middle two of the six listed, these being very similar in value either way. Likewise, the calculations accurately reproduce the absolute lengths of the C–N bonds between the triazine ring and the three amine groups. In particular, the bond from C3–N3 (the amine group involved in the inter-sheet H-bond) is substantially longer than the other two similar contacts.

Supplementary Figure S7 shows that all of the C–N contacts shorten on compression, although the variation is small and the melamine molecule may reasonably be described as 'stiff'. Despite subtle differences, there are no noteworthy differences in the compression of any of these strong covalent bonds.

The amine N–H bond lengths are shown in Supplementary Figure S8, again compared with the 14 K experimental values of Cousson *et al.* [10]. The DFT calculations over-estimate the N–H lengths by ~ 2 %; however, the relative distribution of lengths agrees very well with the experimental observations. Both N1–H1 and N1–H2 exhibit the smallest difference in length whereas the N2–H3 and N2–H4 exhibit the largest. The hydrogen atoms that do not form a hydrogen bond (H3 and H6) have N–H lengths around 1 % shorter than the N–H bonds that do participate in a hydrogen bond.

As one would expect in general, compression shortens intermolecular hydrogen bonds, typically causing covalent N–H bonds to become longer, and this is true of all but one of the N–H bonds also involved in a hydrogen bond (N1–H2). The latter covalent bond exhibits a nearly flat pressure dependence (with even a degree of shortening at the highest pressure) more akin to the behaviour of N2–H3 and N3–H6 where there is no hydrogen bond. The N1–H2$\cdots$N4 contact is the longest of the H-bonded intermolecular contacts, perhaps explaining the weakness of the calculated pressure dependence. There are no discontinuities or sharp changes of slope, which would be characteristic new intermolecular contacts being developed. Clearly, up to 20 GPa, the calculations indicate that the intermolecular framework is not significantly altered.

One set of metrics where both we and Shelton *et al.* [22] offer values of sufficient experimental precision to evaluate pressure dependencies is in the H-bonded N$\cdots$N distances (Figure 9). The DFT calculations give distances that are ~ 2 % shorter than observed experimentally. Nonetheless, the pattern of relative lengths and the magnitudes of the pressure dependencies are once again in agreement with experiment.

Figure 9, Figure 10

Finally, Figure 10 shows the pressure dependence of the angle α, which is the angle between adjacent melamine molecules in any ribbon running along the *b*-axis (*cf.*, Fig. 2), and which defines the corrugation of the melamine sheets. Evidently, the experimental values are very noisy but there is a weakly realised trend of decreasing α under compression that is more precisely defined by the DFT calculations. The decrease in α therefore corresponds with a very slight flattening of the corrugation; given the stiffness of the melamine molecules, this amounts to a force working to lengthen the ribbons along *b*. In part, therefore, the much higher stiffness of K_2 (parallel to *b*) relative to K_3 (perpendicular to *b*) may be due to a component of negative compressibility imbued by the lateral expansion of the sheet as it becomes flattened.

5. Conclusions

We have made accurate and precise determination of the unit-cell parameters of deuterated melamine up to 5 GPa at room pressure, confirming that there are no phase transformations and providing an excellent complement to recent diamond-anvil-cell studies. It is now certain that prior reports of phase transitions at pressures 1 or 2 GPa were incorrect and purported structures based on those data are not likely to be real. Subtle difference in the elastic strain tensor between our work and literature data indicate avenues for further study, either by resonant ultrasonic spectroscopy or additional high-pressure diffraction work. Our measurements as a function of temperature at ambient pressure provide the first measurements of the temperature-dependence of the thermal expansion. Van der Waals-corrected density-functional theory calculations so far provide the only means to accurately and precisely characterise how *all* elements of the structure evolve with pressure; efforts to carry out single-crystal neutron diffraction studies as a function of both *P* and *T* would be beneficial.

Data Availability Statement

Raw data were generated at the ISIS Neutron and Muon Facility are available from the corresponding author [ADF] on request. The authors confirm that the processed data necessary to support the findings of this study are available within the article [and/or] its supplementary materials.

Disclosure statement

No potential conflict of interest was reported by the authors

References

[1]   Zerkowski, J.A., Seto, C.T., & Whitesides, G.M. (1992). Solid-state structures of rosette and crinkled tape motifs derived from the cyanuric acid melamine lattice. *J. Am. Chem. Soc.*, **114**, 5473–5475.

[2]   Tukada, H., & Mazaki, Y. (1997). Cocrystals of melamine and succinimide: supramolecular lattice structure constructed with both self and not-self intermolecular hydrogen bonds. *Chem. Lett*, **26**, 441–442.

[3]   Ranganathan, A., Pedireddi, V.R., & Rao, C.N.R. (1999). Hydrothermal synthesis of organic channel structures: 1: 1 hydrogen-bonded adducts of melamine with cyanuric and trithiocyanuric acids. *J. Am. Chem. Soc.*, **121**, 1752–1753.

[4]   Prior, T.J., Armstrong, J.A., Benoit, D.M., & Marshall, K.L. (2013). The structure of the melamine–cyanuric acid co-crystal. *CrystEngComm*, **15**, 5838–5843.

[5]   Hughes, E.W. (1941). The crystal structure of melamine. *J. Am. Chem. Soc.,* **63**, 1737–1752.

[6]   Larson, A.C., & Cromer, D.T. (1974). Crystal structure refinements with generalized scattering factors. II. Melamine, 2,4,6-triamino-s-triazine. *J. Chem. Phys.*, **60**, 185–192.

[7]   Cromer, D., Larson, A., & Stewart, R. (1975). Refinement of crystal-structure of melamine, 2,4,6-triamino-s-triazine, using generalized scattering factors at octupole level. *Acta Cryst. A*, **31**, S224–S224).

[8]   Cromer, D.T., Larson, A.C., & Stewart, R.F. (1976). Crystal structure refinements with generalized scattering factors. III. Refinement of 1,1′-azobiscarbamide and

melamine, 2,4,6-triamino-s-triazine, at the octopole level. *J. Chem. Phys.*, **65**, 336–349.

[9]   Varghese, J.N., O'Connell, A.M., & Maslen, E.N. (1977). The X-ray and neutron crystal structure of 2, 4, 6-triamino-1, 3, 5-triazine (melamine). *Acta Cryst.B.*, **33**, 2102-2108.

[10]   Cousson, A., & Fillaux, F. (2005). Melamine (1,3,5-triazine-2,4,6-triamine): a neutron diffraction study at 14 K. *Acta Cryst. E*, **61**, o222–o224.

[11]   Etter, M.C., MacDonald, J.C., & Bernstein, J. (1990). Graph-set analysis of hydrogen-bond patterns in organic crystals. *Acta Cryst. B.*, **46**, 256–262.

[12]   Desiraju, G.R., & Gavezzotti, A. (1989). Crystal structures of polynuclear aromatic hydrocarbons. Classification, rationalization and prediction of molecular structure. *Acta Cryst. B*, **45**, 473–482.

[13]   Haussühl, S. (2001). Elastic and thermoelastic properties of selected organic crystals: acenaphthene, trans-azobenzene, benzophenone, tolane, trans-stilbene, dibenzyl, diphenyl sulfone, 2, 2′-biphenol, urea, melamine, hexogen, succinimide, pentaerythritol, urotropine, malonic acid, dimethyl malonic acid, maleic acid, hippuric acid, aluminium acetylacetonate, iron acetylacetonate, and tetraphenyl silicon. *Z. Krist.*, **216**, 339–353.

[14]   Ma, H.A., Jia, X.P., Chen, L.X., Zhu, P.W., Guo, W.L., Guo, X.B., Wang, Y. D., Li, S.Q., Zou, G.T., & Bex, P. (2002). High-pressure pyrolysis study of $C_3N_6H_6$: a route to preparing bulk C_3N_4. *J. Phys. Cond. Matt.*, **14**, 11269.

[15]   Wu. X., Tao, Y., Lu, Y., Dong, L., & Hu, Z. (2006). High-pressure pyrolysis of melamine route to nitrogen-doped conical hollow and bamboo-like carbon nanotubes. *Diamond Rel. Matt.* **15**, 164–170.

[16]   Ma, H.A., Jia, X., Cui, Q.L., Pan, Y.W., Zhu, P.W., Liu, B.B., Liu, H.J., Wang, X.C., & Zou, G.T. (2003). Crystal structures of $C_3N_6H_6$ under high pressure. *Chem. Phys. Lett.*, **368**, 668–672.

[17]   Liu, X. R., Zinin, P. V., Ming, L. C., Acosta, T., Sharma, S. K., Misra, A. K., & Hong, S. M. (2010). Raman spectroscopy of melamine at high pressures. *J. Phys. Conf. Ser.*, **215**, 012045.

[18]   Odake, S., Zinin, P.V., & Ming, L.C. (2013). Raman spectroscopy of melamine at high pressures up to 60 GPa. *High Press. Res.*, **33**, 392–398.

[19] Pravica, M., Kim, E., Tkachev, S., Chow, P., & Xiao, Y. (2010). High-pressure studies of melamine. *High Press. Res.*, **30**, 65–71.

[20] Pravica, M., Galley, M., Park, C., Ruiz, H., & Wojno, J. (2011). In-situ synchrotron x-ray study of phase transitions in melamine under high pressures and high temperatures. *Diamond Rel. Matt.* **20**, 1090–1092.

[21] Galley, M., Pravica, M., & Liu, Z. (2013). High pressure investigations of melamine. *High Press. Res.*, **33**, 40–54.

[22] Shelton, H., Dera, P., & Tkachev, S. (2018). Evolution of interatomic and intermolecular interactions and polymorphism of melamine at high pressure. *Crystals*, **8**, article 265.

[23] Fortes, A.D. (2018a). *Low-T behaviour of melamine*, 1890073, STFC ISIS Facility, doi:10.5286/ISIS.E.91922702

[24] Ibberson, R.M., David, W.I.F., & Knight, K.S. (1992). The high resolution neutron powder diffractometer (HRPD) at ISIS – a user guide. RAL-92-031. Rutherford Appleton Laboratory, U.K.

[25] Ibberson, R.M. (2009). Design and performance of the new supermirror guide on HRPD at ISIS. *Nucl. Instr. Meth. Phys. Res. A.*, **600**, 47–49.

[26] Fortes, A.D. (2018b). Accurate and precise lattice parameters of H_2O and D_2O ice Ih between 1.6 and 270 K from high-resolution time-of-flight neutron powder diffraction data. *Acta Cryst. B.,* **74**, 196–216.

[27] Fortes, A.D., & Capelli, S.C. (2018). H/D isotope effect on the molar volume and thermal expansion of benzene. *Phys. Chem. Chem. Phys.*, **20**, 16736–16742.

[28] Mantid (2013). Manipulation and Analysis Toolkit for Instrument Data; Mantid Project. http://dx.doi.org/10.5286/SOFTWARE/MANTID.

[29] Arnold, O., & 27 co-authors (2014). Mantid—Data analysis and visualization package for neutron scattering and μSR experiments. *Nucl. Instrum. Methods Phys. Res. A*, **764**, 156–166.

[30] Fortes, A.D. (2018c). *Phase transitions in melamine at high pressure*, 1810003, STFC ISIS Facility, doi:10.5286/ISIS.E.90605896

[31] Bull, C.L., Funnell, N.P., Tucker, M.G., Hull, S., Francis, D.J., & Marshall, W.G. (2016). PEARL: the high pressure neutron powder diffractometer at ISIS. *High Press. Res.*, **36**, 493–511.

[32] Marshall, W.G., & Francis, D.J. (2002). Attainment of near-hydrostatic compression conditions using the Paris-Edinburgh cell. *J. Appl. Cryst*. **35**, 122–125.

[33]   Fortes, A.D. (2019). A revised equation of state for *in situ* pressure determination using fcc-Pb (0 < P < 13 GPa, T > 100 K). RAL Technical Report TR–2019–002.

[34]   Hohenberg, P., & Kohn, W. (1964). Inhomogeneous electron gas. *Phys. Rev.*, **136**, B864–B871.

[35]   Kohn, W., & Sham, L.J. (1965). Self-consistent equations including exchange and correlation effects. *Phys. Rev.*, **140**, A1133.

[36]   Payne, M.C., Teter, M.P., Allan, D.C., Arias, T.A., & Joannopoulos, A.J. (1992). Iterative minimization techniques for ab initio total-energy calculations: molecular dynamics and conjugate gradients. *Rev. Mod. Phys.*, **64**, 1045.

[37]   Segall, M.D., Lindan, P.J., Probert, M.A., Pickard, C.J., Hasnip, P.J., Clark, S.J., & Payne, M.C. (2002). First-principles simulation: ideas, illustrations and the CASTEP code. *J. Phys. Cond. Matt.*, **14**, 2717.

[38]   Clark, S.J., Segall, M.D., Pickard, C.J., Hasnip, P.J., Probert, M.I., Refson, K., & Payne, M.C. (2005). First principles methods using CASTEP. *Z. Krist.* **220**, 567–570.

[39]   Perdew, J.P., Burke, K., & Ernzerhof, M. (1996). Generalized gradient approximation made simple. *Phys. Rev. Lett.*, **77**, 3865.

[40]   Tkatchenko, A., & Scheffler, M. (2009). Accurate molecular van der Waals interactions from ground-state electron density and free-atom reference data. *Phys. Rev. Lett.*, **102**, 073005.

[41]   Larson, A.C. & Von Dreele, R.B. (1994). General Structure Analysis System (GSAS). Los Alamos National Laboratory Report, LAUR 86-748.

[42]   Toby, B.H. (2001). EXPGUI, a graphical user interface for GSAS. *J. Appl. Cryst.,* **34**, 210–213.

[43]   Albinati, A., & Willis, B. T. M. (1982). The Rietveld method in neutron and X-ray powder diffraction. *J. Appl. Cryst.,* **15**, 361–374.

[44]   Le Bail, A. (2005). Whole powder pattern decomposition methods and applications: A retrospection. *Powder Diff.*, **20**, 316–326.

[45]   Angel, R.J., Gonzalez-Platas, J., Alvaro, M. (2014). EosFit-7c and a Fortran module (library) for equation of state calculations. *Z. Krist.*, **229**, 405–419.

[46]   Birch, F. (1952). Elasticity and constitution of the Earth's interior. *J. Geophys. Res.*, **57**, 227–286.

[47]   Murnaghan, F. D. (1944). The compressibility of media under extreme pressures. *Proc. Natl. Acad. Sci.*, **30**, 244–247.

[48] Fortes, A.D., Wood, I.G., Alfredsson, M., Vočadlo, L., & Knight, K.S. (2006). The thermoelastic properties of $MgSO_4 \cdot 7D_2O$ (epsomite) from powder neutron diffraction and *ab initio* calculation. *Eur. J. Min.,* **18**, 449–462.

[49] Fortes, A.D., Wood, I.G., Vočadlo, L., Knight, K.S., Marshall, W.G., Tucker, M.G., & Fernandez-Alonso, F. (2009). Phase behaviour and thermoelastic properties of perdeuterated ammonia hydrate and ice polymorphs from 0 to 2 GPa. *J. Appl Cryst.,* **42**, 846–866.

[50] Fortes, A.D., Wood, I.G., Tucker, M.G., & Marshall, W.G. (2012). The P–V–T equation of state of D_2O ice VI determined by neutron powder diffraction in the range 0< P< 2.6 GPa and 120< T< 330 K, and the isothermal equation of state of D_2O ice VII from 2 to 7 GPa at room temperature. *J. Appl Cryst.,* **45**, 523–534.

[51] Fortes, A.D., Brand, H.E.A., Vočadlo, L., Lindsay-Scott, A., Fernandez-Alonso, F., & Wood, I.G. (2013). P–V–T equation of state of synthetic mirabilite ($Na_2SO_4 \cdot 10D_2O$) determined by powder neutron diffraction. *J. Appl Cryst.,* **46**, 448–460.

[52] Klotz, S., Komatsu, K., Kagi, H., Kunc, K., Sano-Furukawa, A., Machida, S., & Hattori, T. (2017). Bulk moduli and equations of state of ice VII and ice VIII. *Phys. Rev. B* **95**, 174111.

Figure Captions

Figure 1

Geometry and atom-labelling scheme of the melamine molecule and its hydrogen bonding to nearest neighbours within the (*201*)-coplanar corrugated sheet. Hydrogen bonds are denoted by dashed rods. The underlined hydrogen atoms form no hydrogen bond; H5 participates in a hydrogen bond (shown on Figure 2) with the triazine N5 atom in an adjacent sheet. Symmetry codes: (i) ½−x, y−½, −z; (ii) −x, −1−y, 1−z; (iii) ½−x, ½+y, −z.

Figure 2

Larger scale connectivity and packing of melamine into ribbons and sheets, which are vertically stacked to form the complete crystal structure.

Figure 3

Stackplot of neutron powder diffraction patterns measured on PEARL as a function of pressure. The region depicted is the high d-spacing half of the diffraction pattern, with strong and well-resolved peaks from the melamine-d6 sample, the Pb pressure marker and the alumina anvils (Miller indices of certain Bragg peaks are marked). The vertical dispersion of the patterns is linear in *P*, the uneven appearance being due to variations in the load-pressure curve and changes in load increment as the experiment progressed.

Figure 4

Temperature dependence of the lattice parameters of melamine-d6 refined from powder diffraction data measured on HRPD, compared with values from Cousson *et al*. [10]. The solid lines represent a power/exponential model fitted to the data (see text).

Figure 5

Pressure dependence of the lattice parameters of melamine-d6 refined from powder diffraction data measured on PEARL, compared with values from Shelton *et al*. [22]. The solid lines represent a 3rd order Birch-Murnaghan equation of state fitted to the data (see text).

Figure 6

Derived volume thermal expansion (top left), principal magnitudes of the thermal expansion tensor (top right), and the angle between the α_1 direction and the normal to the (*201*) plane

(bottom left). The bottom right diagram depicts a section through the thermal expansion tensor representation glyph perpendicular with α_2, defining the angle φ.

Figure 7

Pressure dependence of the compressibility tensor coefficients, ε_{ij}.

Figure 8

Three dimensional tensor representation glyphs describing the thermal expansion at 297 K (left) and compressibility at 0 GPa (right). The unit-cell of the crystal and the principal strain directions of each tensor are marked by arrows; the light blue sheet in the middle of the unit cell is parallel with the (*201*) family of planes in the crystal.

Figure 9

Calculated variation of the hydrogen-bonded intermolecular N–H···N contacts, compared (at the same volumes) with experimental data derived from this work and the single-crystal X-ray diffraction study of Shelton *et al*. [22]. The bottom right panel shows the inter-sheet contact; the other three panels each report in-sheet distances.

Figure 10

Calculated variation of the angle, α, between adjacent melamine molecules in a ribbon running along the *b*-axis, defining a corrugation of the (*201*)-coplanar sheets (see Figure 2).

Tables

Table 1:

Comparison of the low-temperature lattice parameters of melamine from different sources.

	HRPD 4.2 K	DFT 0 K	Difference (%)	HRPD 15 K	[Ref. 10] 14 K	Difference (%)
a (Å)	10.4477	10.5530	+1.01	10.4483	10.433	−0.15
b (Å)	7.4561	7.40227	−0.72	7.4560	7.458	+0.03
c (Å)	7.2433	7.15285	+1.25	7.2433	7.238	−0.07
β (°)	113.376	113.145	−0.20	113.374	113.30	−0.07
V (Å^3)	517.934	513.781	−0.80	517.965	517.30	−0.13

Table 2:

Parameters obtained by fitting Eq. 1 to the experimental data.

	a-axis (Å)	b-axis (Å)	c-axis (Å)	β (°)	V (Å^3)
X_0	10.4482(1)	7.45589(6)	7.24330(7)	113.373(1)	517.94(1)
p	0.20(1)	$1.8(7) \times 10^{-2}$	$5.3(4) \times 10^{-2}$	$-1.76(9)$	23.4(8)
q	$-50(1)$	$-55(6)$	$-45(2)$	$-48(1)$	$-49.4(7)$
r	$9.8(4) \times 10^{-4}$	$1.72(3) \times 10^{-4}$	$2.9(2) \times 10^{-4}$	$-6.5(2) \times 10^{-3}$	0.111(2)
s	$-486(24)$	$-353(37)$	$-477(34)$	$-462(25)$	$-486(15)$

Table 3:

Parameters obtained by fitting a 3rd order Birch-Murnaghan equation of state to the experimental data.

	a (Å)	b (Å)	c (Å)	V (Å^3)
X_0	10.6064(6)	7.48451(3)	7.298(3)	536.7(6)
$K_{0,x}$	33.7(8)	156(3)	37(1)	12.0(5)
K'	29(1)	41(3)	19(1)	7.8(5)

Figure 1

Figure 2

intersheet R$_2^2$(8)

α

R$_2^2$(8) tape

zipper

R$_2^2$(8) tape

flat
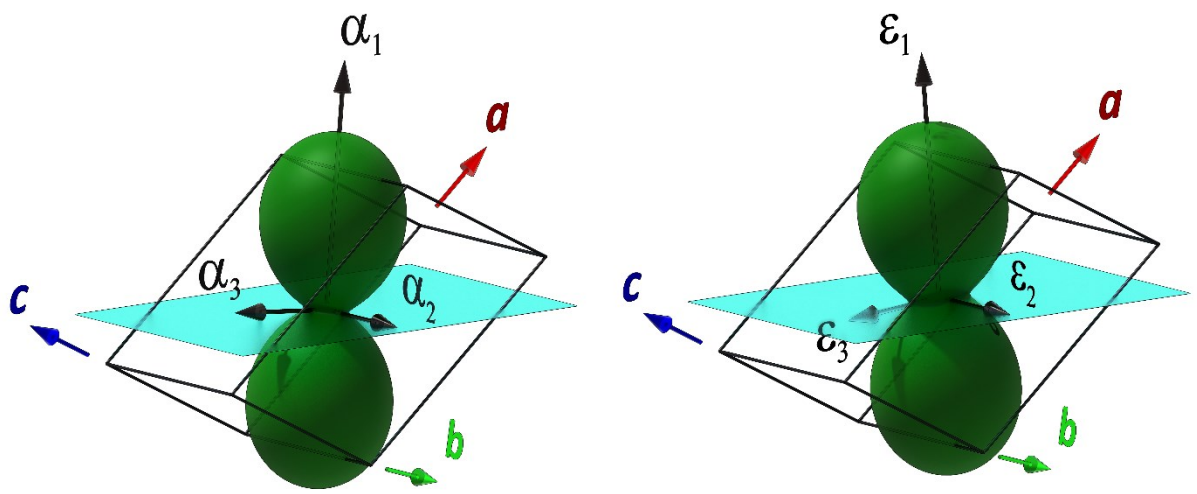
corrugated
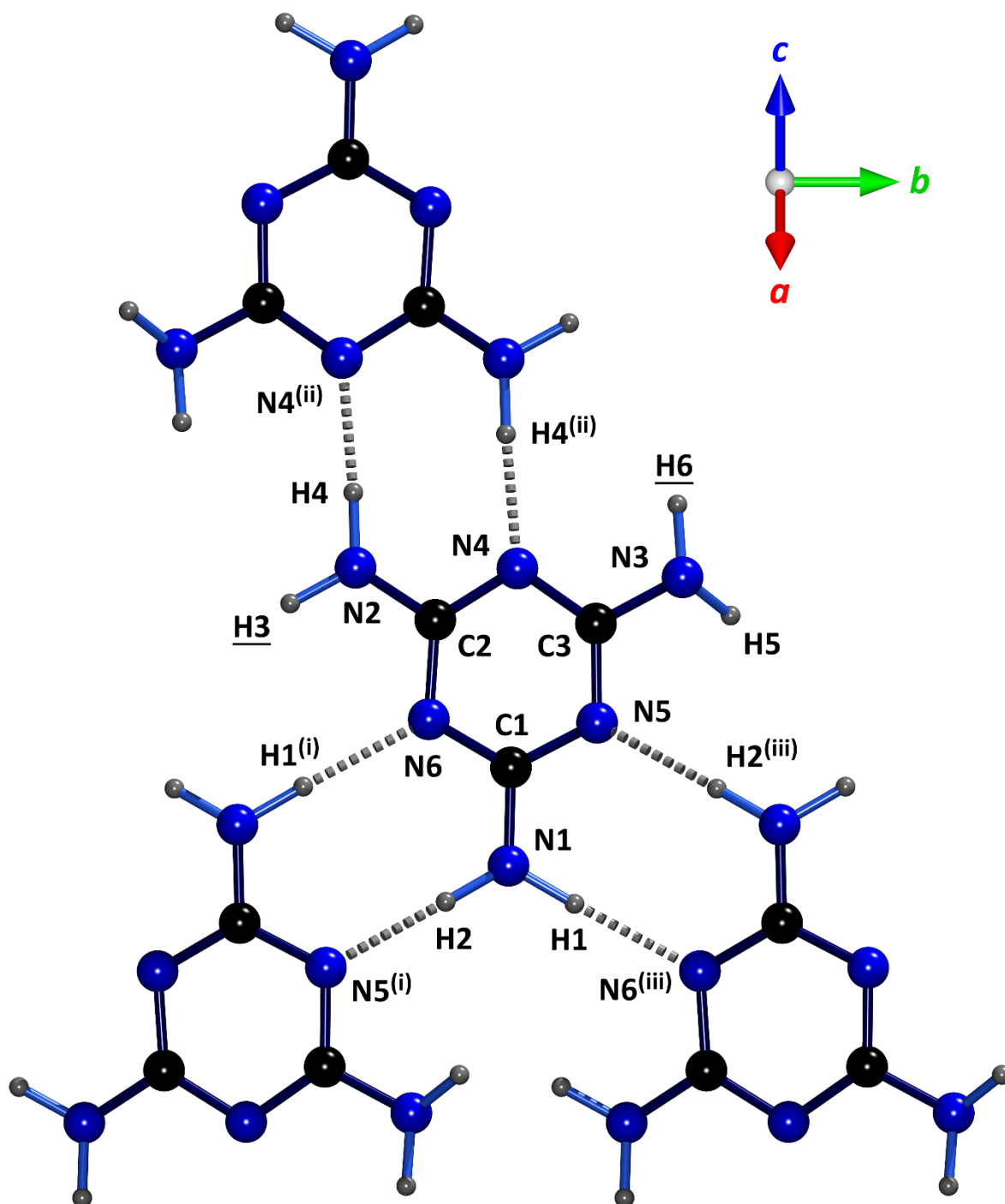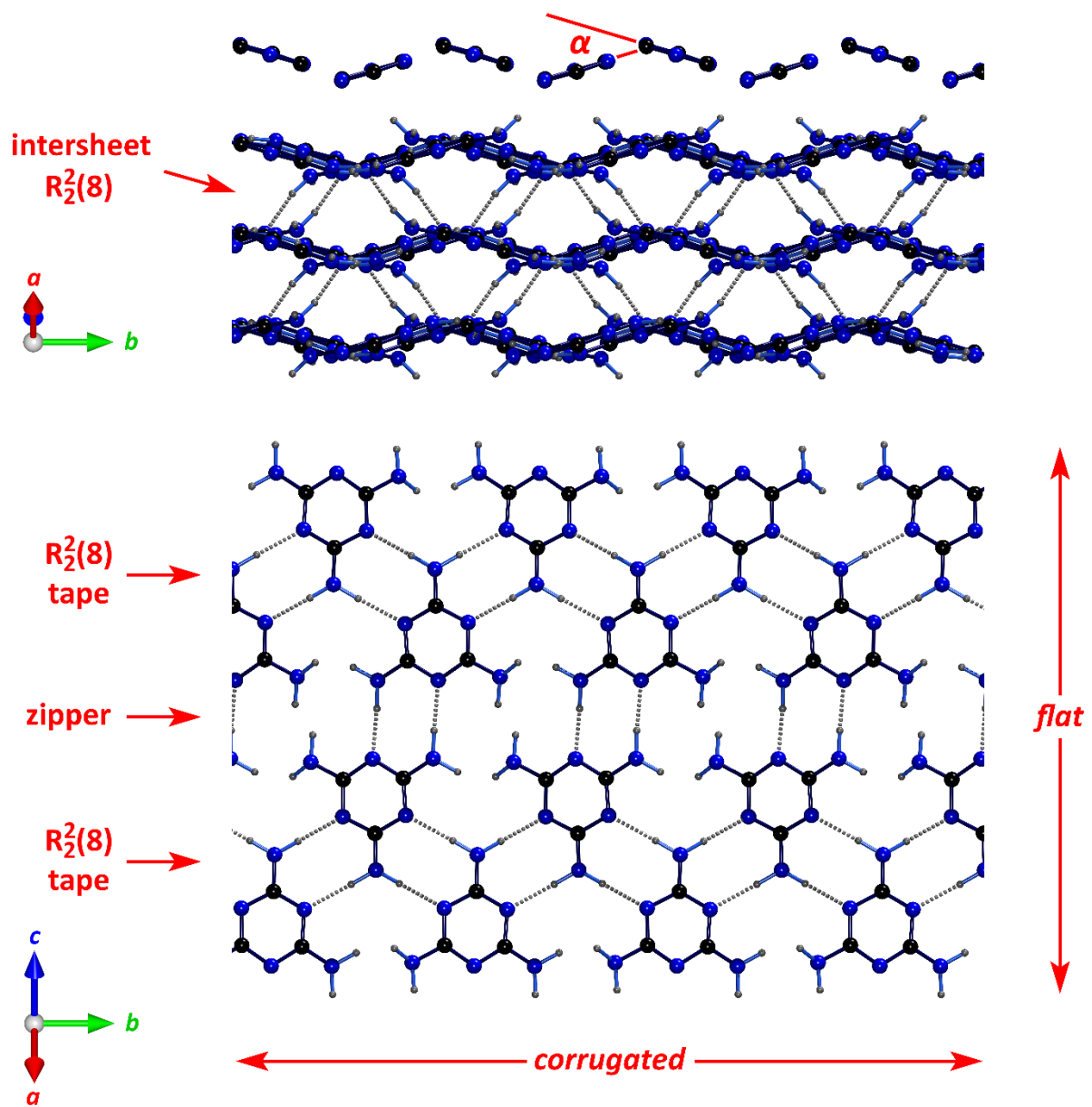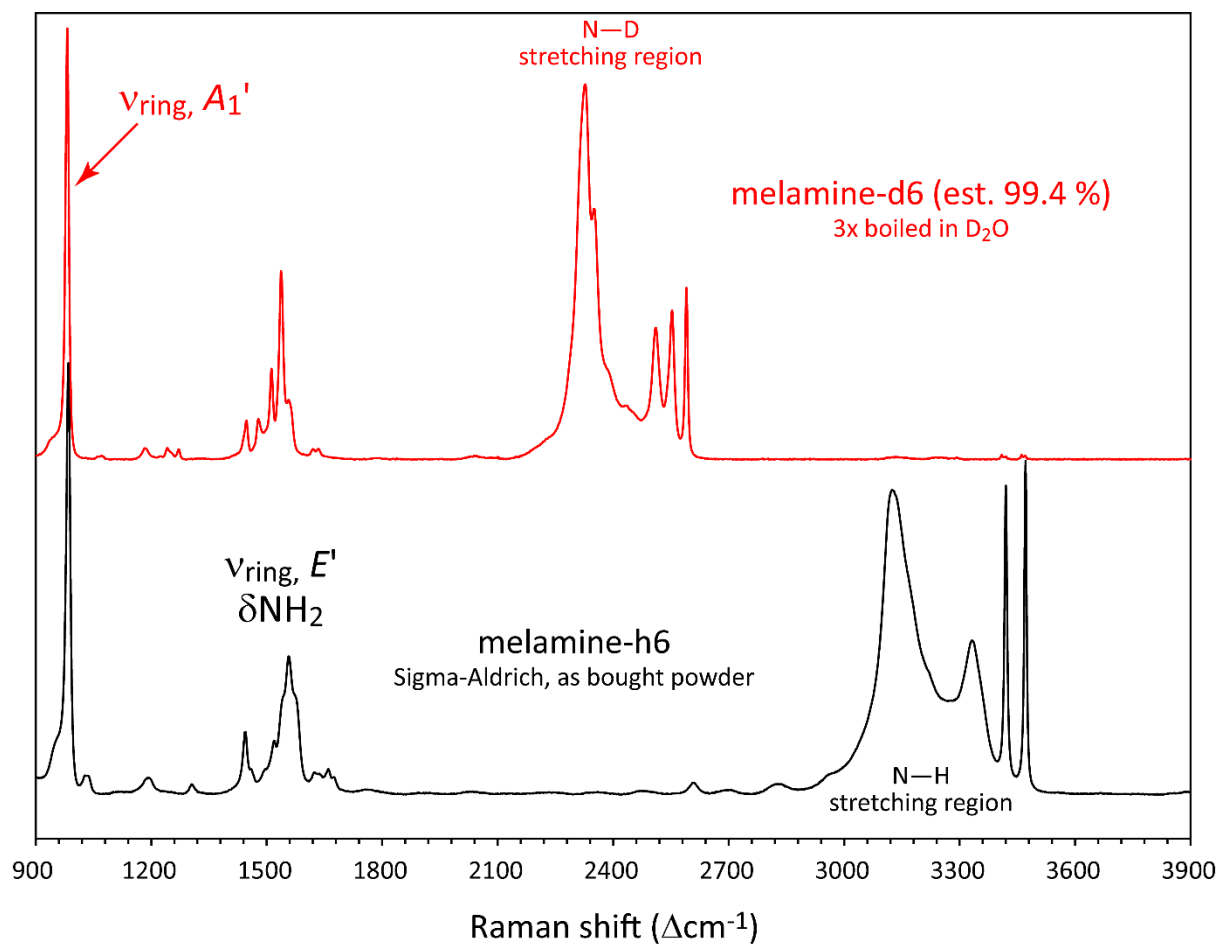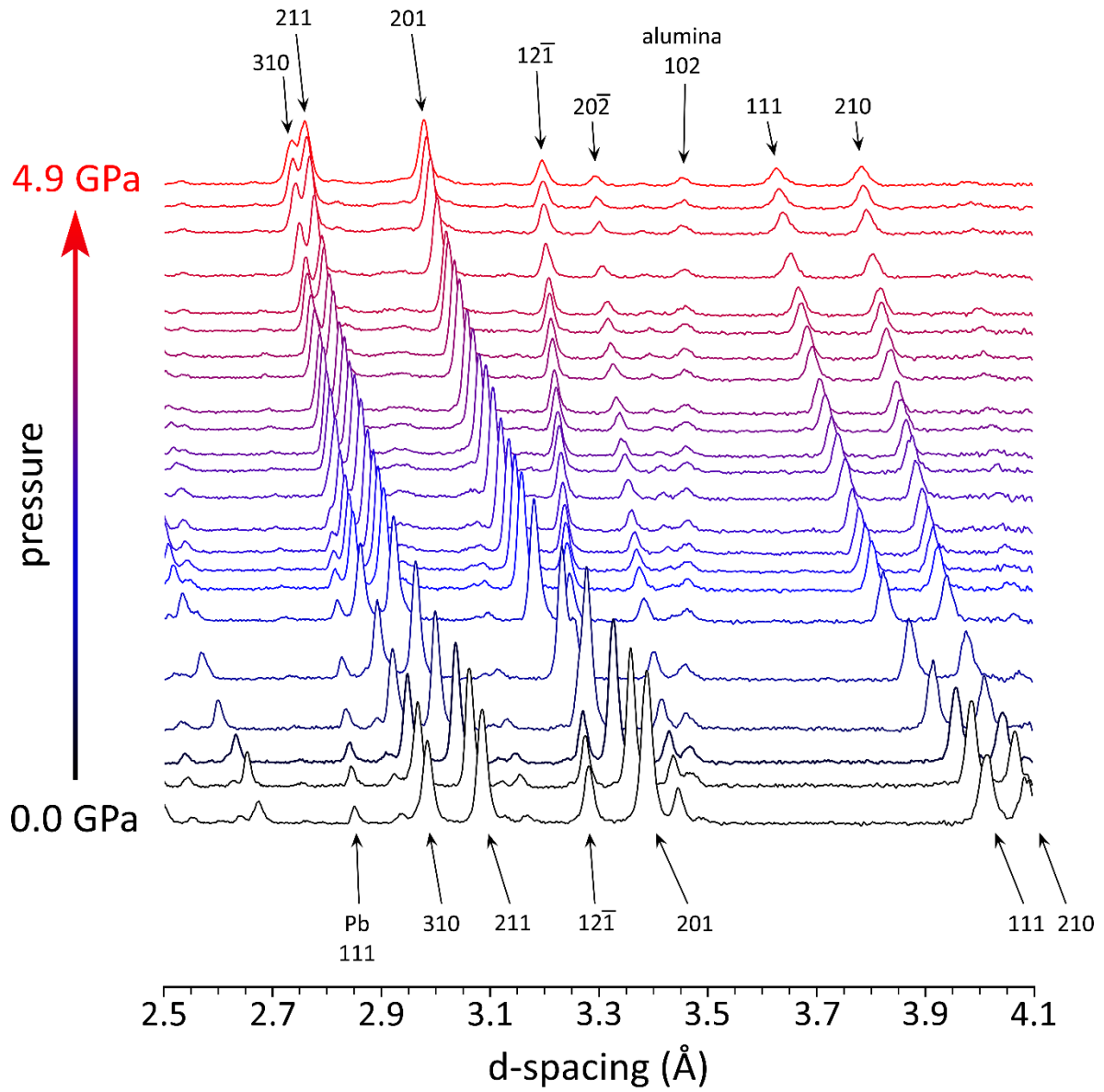
Figure 3

Figure 4
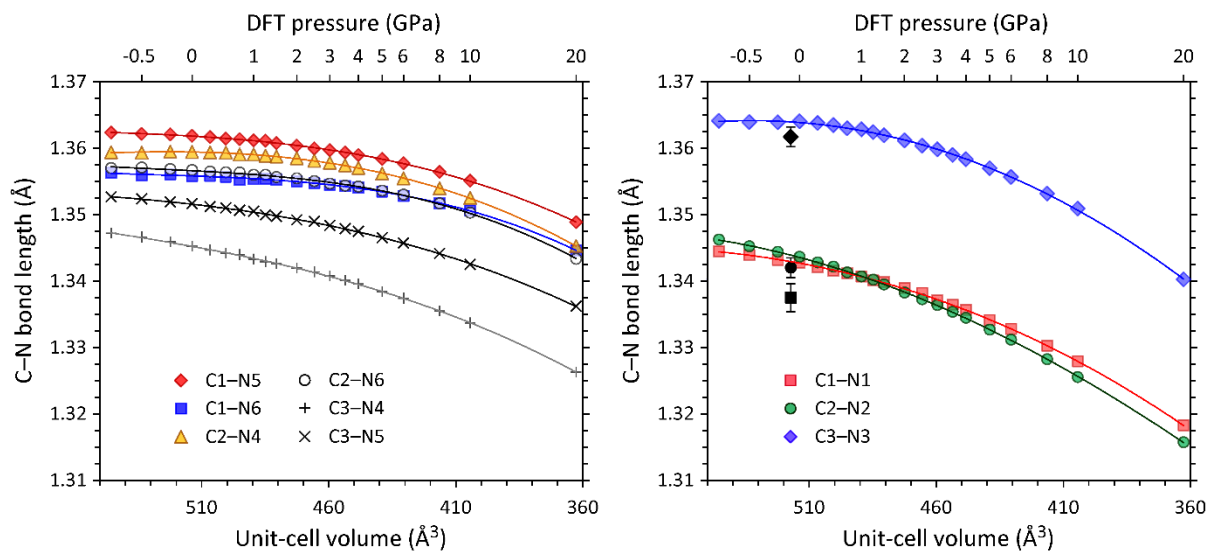
Figure 5
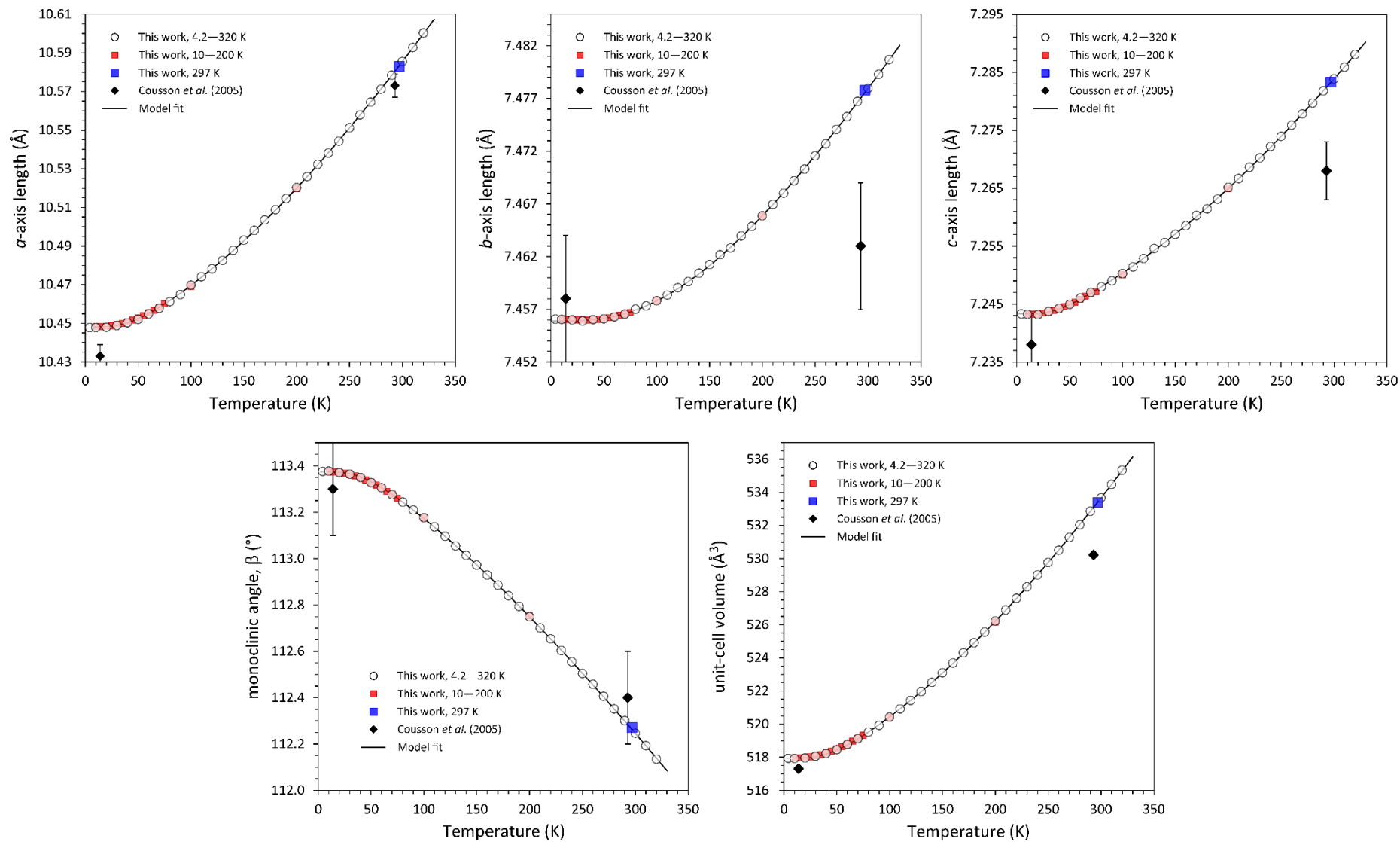
Figure 6
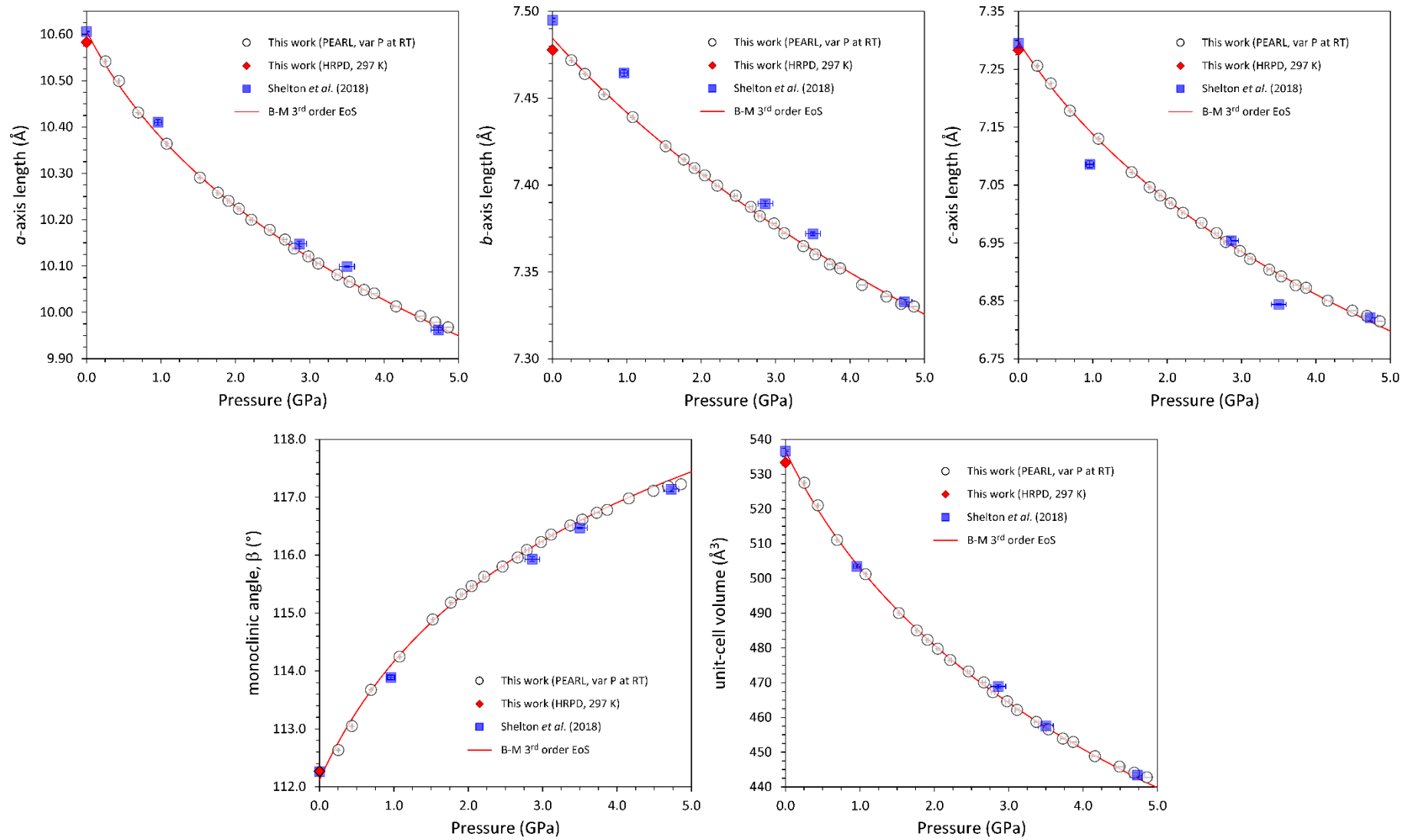
Figure 7
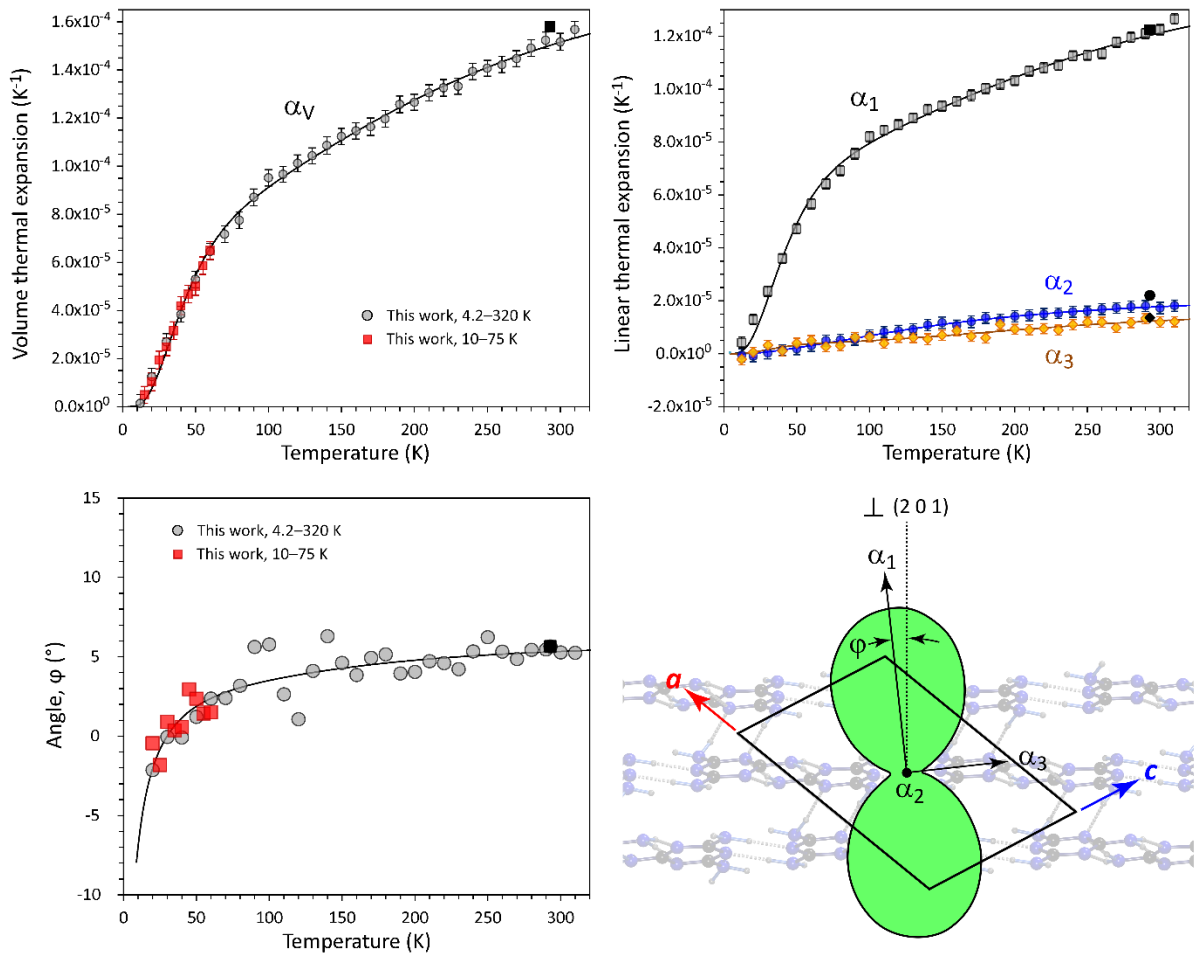
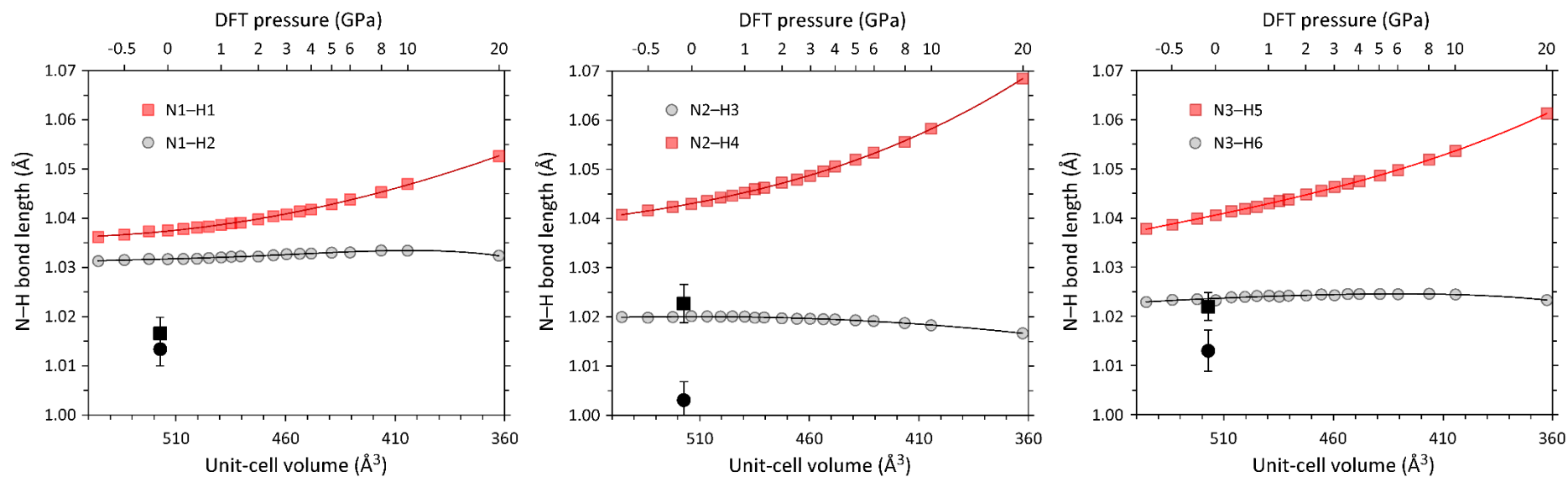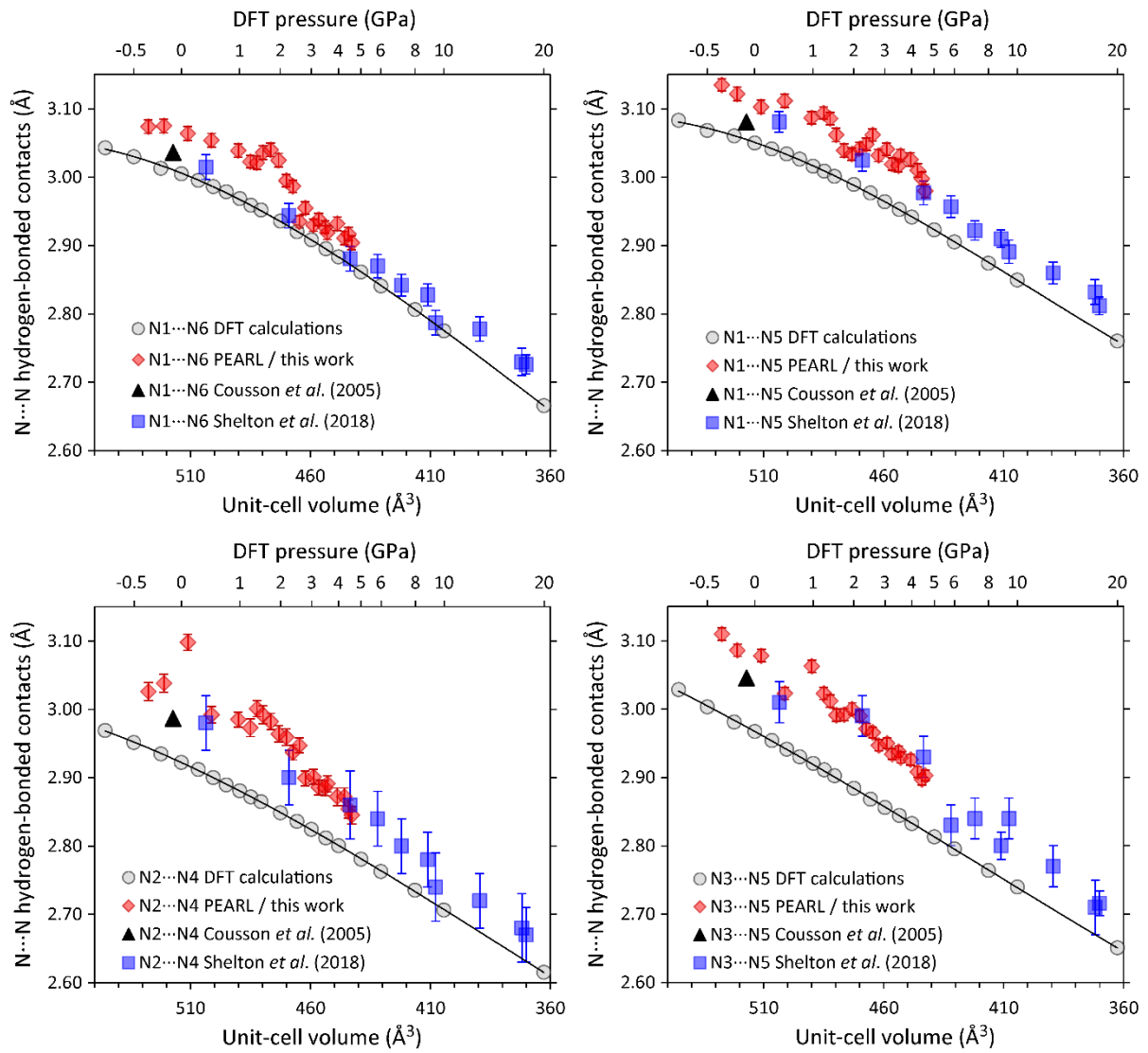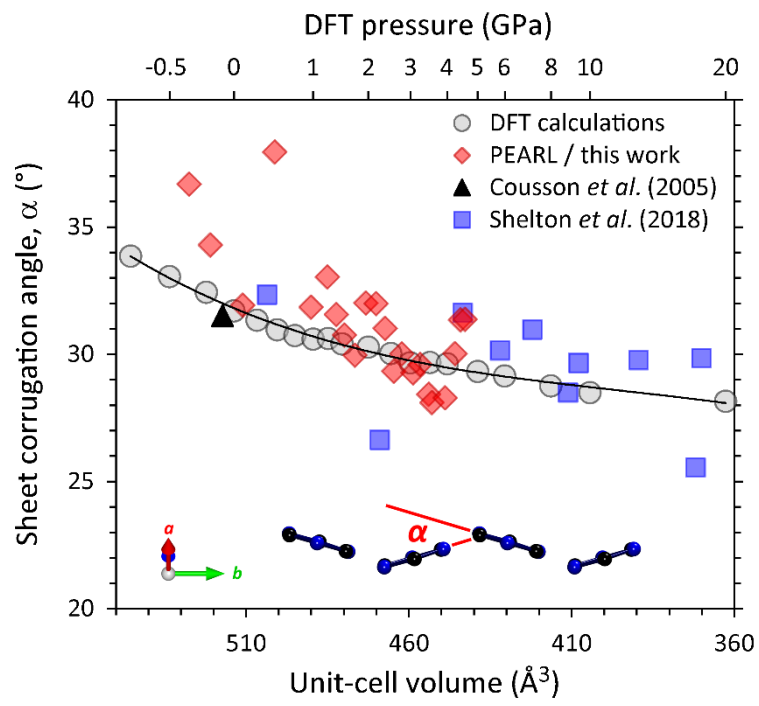Figure 8
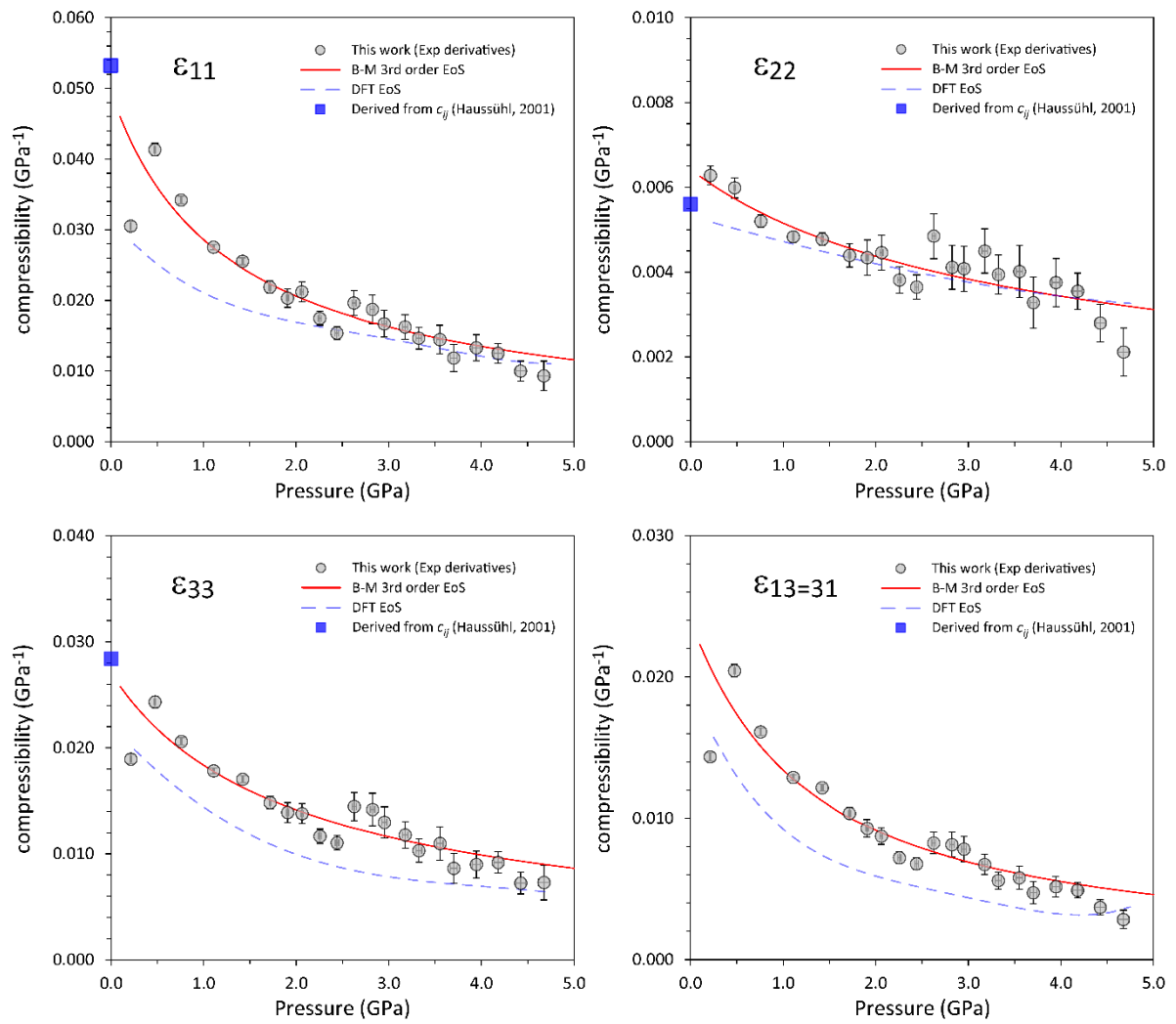
Figure 9

Figure 10

Figure 11

Figure 12

Figure 13

Electronic Supplementary Information

Thermoelastic properties of deuterated melamine, $C_3N_6D_6$, between 4.2 – 320 K at 5 kPa and between 0.1 – 5.0 GPa at 295 K from neutron powder diffraction and DFT calculations.

A. D. Fortes,[1*] N. P. Funnel,[1] and C. L. Bull[1]

[1]ISIS Neutron Spallation Souce, Rutherford Appleton Laboratory, Harwell Science and Innovation Campus, Chilton, Oxfordshire OX11 0QX, U. K.

Corresponding author: dominic.fortes@stfc.ac.uk

CONTENTS

Table S1

Refined lattice parameters as a function of temperature from neutron powder diffraction data measured on HRPD.

T (K)	a (Å)	b (Å)	c (Å)	β (°)	V (Å^3)
4.22	10.44774(10)	7.45606(3)	7.24332(8)	113.376(1)	517.934(6)
10	10.44779(13)	7.45603(4)	7.24323(11)	113.377(1)	517.925(8)
20	10.44789(13)	7.45599(4)	7.24317(10)	113.371(1)	517.945(7)
30	10.44883(12)	7.45589(4)	7.24373(10)	113.364(1)	518.053(7)
40	10.45026(13)	7.45602(4)	7.24425(11)	113.350(1)	518.225(8)
50	10.45198(13)	7.45609(4)	7.24495(10)	113.328(1)	518.452(8)
60	10.45492(13)	7.45628(4)	7.24603(10)	113.306(1)	518.774(7)
70	10.45781(14)	7.45654(4)	7.24699(10)	113.276(1)	519.120(8)
80	10.46119(14)	7.45701(4)	7.24799(11)	113.244(1)	519.517(8)
90	10.46479(14)	7.45732(4)	7.24903(10)	113.210(1)	519.923(7)
100	10.46975(13)	7.45781(4)	7.25025(10)	113.177(1)	520.421(8)
110	10.47411(14)	7.45834(4)	7.25142(10)	113.137(1)	520.913(8)
120	10.47817(13)	7.45903(4)	7.25286(10)	113.096(1)	521.426(8)
130	10.48252(14)	7.45962(4)	7.25460(11)	113.055(1)	521.968(9)
140	10.48773(13)	7.46041(4)	7.25561(10)	113.014(1)	522.514(8)
150	10.49305(13)	7.46123(4)	7.25703(10)	112.972(1)	523.100(8)
160	10.49802(14)	7.46216(4)	7.25851(11)	112.929(1)	523.689(9)
170	10.50347(13)	7.46282(4)	7.26030(11)	112.886(1)	524.304(8)
180	10.50882(14)	7.46396(4)	7.26142(11)	112.840(1)	524.911(9)
190	10.51455(13)	7.46484(4)	7.26313(10)	112.794(1)	525.559(9)
200	10.52024(13)	7.46586(4)	7.26514(10)	112.750(1)	526.228(8)
210	10.52594(13)	7.46695(4)	7.26665(11)	112.701(1)	526.888(8)
220	10.53223(13)	7.46802(4)	7.26860(10)	112.654(1)	527.601(8)
230	10.53808(13)	7.46918(4)	7.27022(10)	112.604(1)	528.287(8)
240	10.54428(13)	7.47030(4)	7.27219(10)	112.555(1)	529.008(8)
250	10.55115(13)	7.47154(4)	7.27394(10)	112.505(1)	529.760(8)
260	10.55782(12)	7.47270(4)	7.27588(10)	112.458(1)	530.500(8)
270	10.56443(13)	7.47406(4)	7.27781(11)	112.406(1)	531.269(8)
280	10.57117(13)	7.47528(4)	7.27967(11)	112.352(1)	532.033(8)
290	10.57844(13)	7.47672(4)	7.28179(11)	112.301(1)	532.854(8)
300	10.58551(13)	7.47797(4)	7.28386(11)	112.247(1)	533.657(8)
310	10.59274(14)	7.47930(4)	7.28589(12)	112.193(1)	534.470(9)
320	10.60027(14)	7.48069(4)	7.28808(11)	112.135(1)	535.330(9)

T (K)	a (Å)	b (Å)	c (Å)	β (°)	V (Å^3)
297	10.58301(7)	7.47779(5)	7.28332(5)	112.272	533.382(4)

T (K)	a (Å)	b (Å)	c (Å)	β (°)	V (Å^3)
10	10.44819(4)	7.456032(8)	7.24323(3)	113.3745(3)	517.954(2)
15	10.44831(6)	7.45603(1)	7.24326(4)	113.3735(3)	517.965(3)
20	10.44841(6)	7.45604(1)	7.24320(4)	113.3714(3)	517.976(3)
25	10.44876(5)	7.45600(1)	7.24345(4)	113.3681(3)	518.020(3)
30	10.44927(5)	7.45596(1)	7.24365(4)	113.3628(3)	518.078(3)
35	10.44989(5)	7.45597(1)	7.24389(4)	113.3568(3)	518.150(3)
40	10.45063(5)	7.45601(1)	7.24418(2)	113.3493(3)	518.240(3)
45	10.45169(5)	7.45605(1)	7.24456(4)	113.3385(3)	518.365(3)
50	10.45284(5)	7.45609(1)	7.24493(4)	113.3299(3)	518.484(3)
55	10.45395(6)	7.45620(1)	7.24532(4)	113.3171(4)	518.626(3)
60	10.45538(6)	7.45631(1)	7.24584(4)	113.3055(4)	518.786(3)
65	10.45679(5)	7.45644(1)	7.24636(4)	113.2903(3)	518.962(3)
70	10.45834(5)	7.45655(1)	7.24690(4)	113.2773(4)	519.136(3)
75	10.46011(6)	7.45670(1)	7.24715(4)	113.2604(4)	519.318(3)
100	10.46918(5)	7.45784(1)	7.25008(3)	113.1758(3)	520.387(2)
200	10.51963(5)	7.46584(1)	7.26490(4)	112.7529(3)	526.168(2)

Table S2:

Refined lattice parameters as a function of pressure from neutron powder diffraction data measured on PEARL.

Load (T)	P (GPa)	a (Å)	b (Å)	c (Å)	β (°)	V (Å3)
0	0.000(6)	10.5876(2)	7.4851(1)	7.2874(2)	112.305(1)	534.30(1)
6	0.255(6)	10.5417(2)	7.4718(2)	7.2560(2)	112.633(1)	527.51(1)
8	0.437(7)	10.4993(3)	7.4640(2)	7.2254(2)	113.048(1)	521.03(1)
10	0.694(7)	10.4310(3)	7.4522(2)	7.1785(2)	113.672(2)	511.06(2)
12	1.078(7)	10.3636(2)	7.4391(1)	7.1299(2)	114.246(1)	501.20(1)
14	1.524(9)	10.2906(2)	7.4223(2)	7.0722(2)	114.887(1)	490.01(1)
16	1.77(1)	10.2581(2)	7.4146(2)	7.0463(2)	115.178(1)	485.02(1)
18	1.91(1)	10.2405(2)	7.4098(1)	7.0318(2)	115.324(1)	482.30(1)
20	2.05(1)	10.2235(3)	7.4055(2)	7.0186(2)	115.465(1)	479.76(1)
22	2.22(2)	10.1996(3)	7.3997(2)	7.0021(2)	115.626(1)	476.49(1)
24	2.46(2)	10.1778(3)	7.3938(2)	6.9847(2)	115.800(2)	473.22(2)
26	2.67(2)	10.1571(2)	7.3875(1)	6.9671(2)	115.957(1)	470.04(1)
28	2.79(2)	10.1376(3)	7.3821(2)	6.9517(2)	116.089(2)	467.24(2)
30	2.98(3)	10.1208(2)	7.3780(2)	6.9362(2)	116.226(1)	464.61(1)
32	3.12(3)	10.1053(2)	7.3723(1)	6.9223(2)	116.353(1)	462.12(1)
35	3.37(3)	10.0811(2)	7.3649(2)	6.9040(2)	116.511(1)	458.70(1)
37.5	3.54(3)	10.0658(2)	7.3601(1)	6.8924(2)	116.612(1)	456.53(1)
40	3.73(4)	10.0483(3)	7.3544(2)	6.8770(2)	116.730(2)	453.89(2)
42.5	3.87(4)	10.0409(4)	7.3521(2)	6.8725(2)	116.782(2)	452.91(2)
52	4.16(5)	10.0126(2)	7.3425(2)	6.8503(2)	116.977(2)	448.82(2)
55	4.49(5)	9.9918(3)	7.3358(2)	6.8332(2)	117.110(2)	445.83(2)
57.5	4.69(6)	9.9787(3)	7.3316(2)	6.8242(2)	117.189(2)	444.09(2)
60	4.86(6)	9.9675(3)	7.3301(2)	6.8148(2)	117.223(2)	442.75(2)

Table S3:

Lattice parameters and total electronic energy per unit cell as a function of pressure from vdW-corrected PBE density-function theory calculations.

P (GPa)	E (eV)	a (Å)	b (Å)	c (Å)	β (°)	V (Å^3)
−0.745	−8762.98	10.75175	7.430003	7.317965	111.0624	545.5422
−0.501	−8763.03	10.66342	7.417326	7.266948	111.8211	533.5891
−0.257	−8763.07	10.60666	7.408938	7.196699	112.5527	522.2968
0.001	−8763.08	10.55297	7.402272	7.152846	113.1446	513.7806
0.248	−8763.08	10.51756	7.391407	7.112533	113.6042	506.6641
0.494	−8763.07	10.47667	7.382992	7.082158	113.9952	500.4577
0.755	−8763.06	10.43852	7.375801	7.055207	114.3081	495.0406
0.998	−8763.03	10.40763	7.361296	7.026958	114.6084	489.4641
1.248	−8763.00	10.37962	7.352379	6.999361	114.8159	484.8322
1.497	−8762.97	10.34594	7.346231	6.979662	115.0516	480.5762
1.996	−8762.89	10.28474	7.329245	6.940881	115.4273	472.5172
2.499	−8762.80	10.22451	7.317155	6.910145	115.7585	465.6080
3.004	−8762.70	10.17564	7.305795	6.882173	116.0672	459.5851
3.500	−8762.59	10.12830	7.288069	6.855354	116.3252	453.5532
4.002	−8762.47	10.08725	7.272923	6.830641	116.5449	448.2957
5.002	−8762.21	10.00709	7.252158	6.786249	116.9726	438.9264
5.999	−8761.93	9.934072	7.230352	6.746653	117.3054	430.5947
7.996	−8761.33	9.805059	7.195878	6.678518	117.9041	416.4230
10.002	−8760.67	9.702051	7.164369	6.614402	118.4109	404.3863
20.004	−8756.92	9.341524	7.043110	6.369243	120.0638	362.6778

Figure S1

The higher-frequency portion of the Raman spectrum of melamine-h6 (bottom) and melamine-d6 prepared from the former by exchange in boiling D_2O (top), confirming the very high degree of deuteration of the material measured in this study.
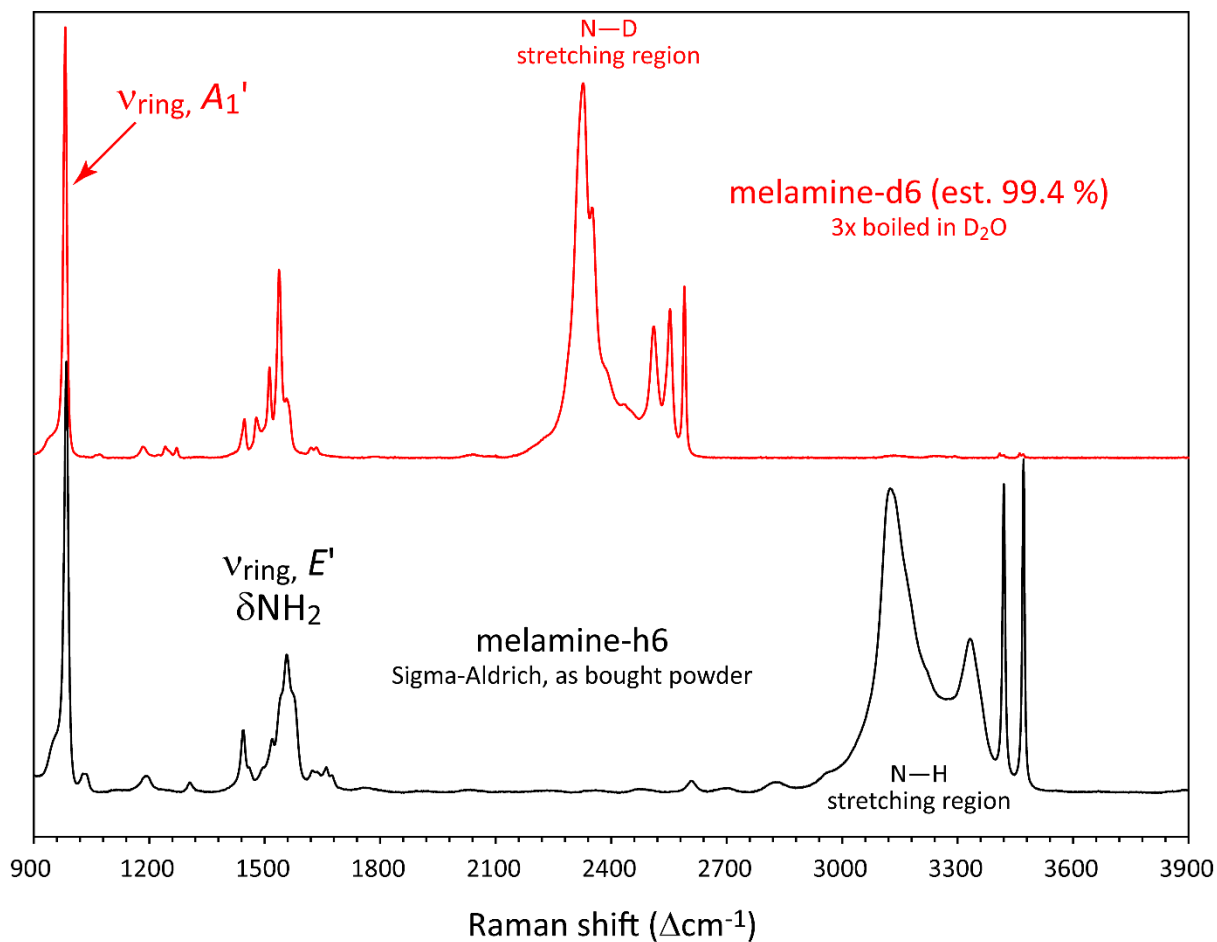
Figure S2

Temperature dependence of the *b*-axis length below 100 K in melamine-d6 showing the small degree of negative expansion (reproduced in both series of HRPD data) below 30 K. The solid line is fit of the power/exponential model (see main text) ignoring the region of negative linear expansion.
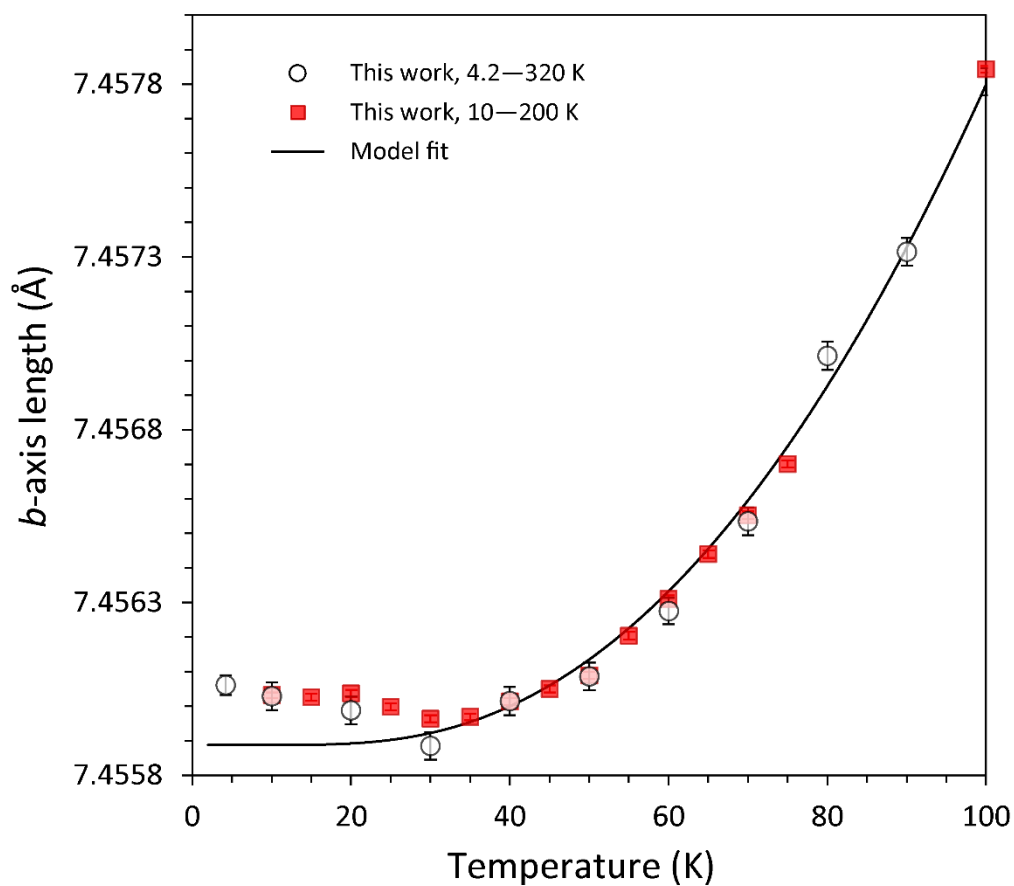
Figure S3

Expanded view of the volume thermal expansion of melamine-d6 below 100 K, principally illustrating the small difference between the two models used to fit the unit-cell volume.
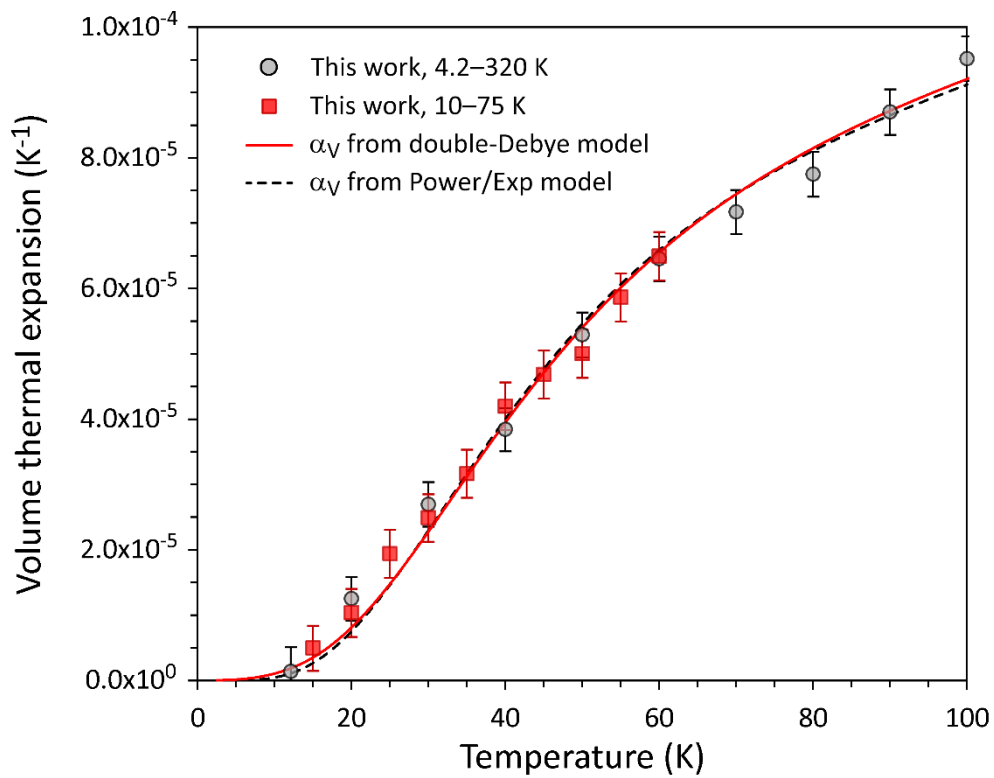
Figure S4

Magnitudes of the principal linear expansivities of melamine-d6, plotted on separate scales to highlight subtleties in the behaviour of each one. At the bottom, the angle between the direction of greatest linear expansion, α_1, and the sheets of melamine molecules in the crystal is plotted, along with a graphic defining the geometric relationships.
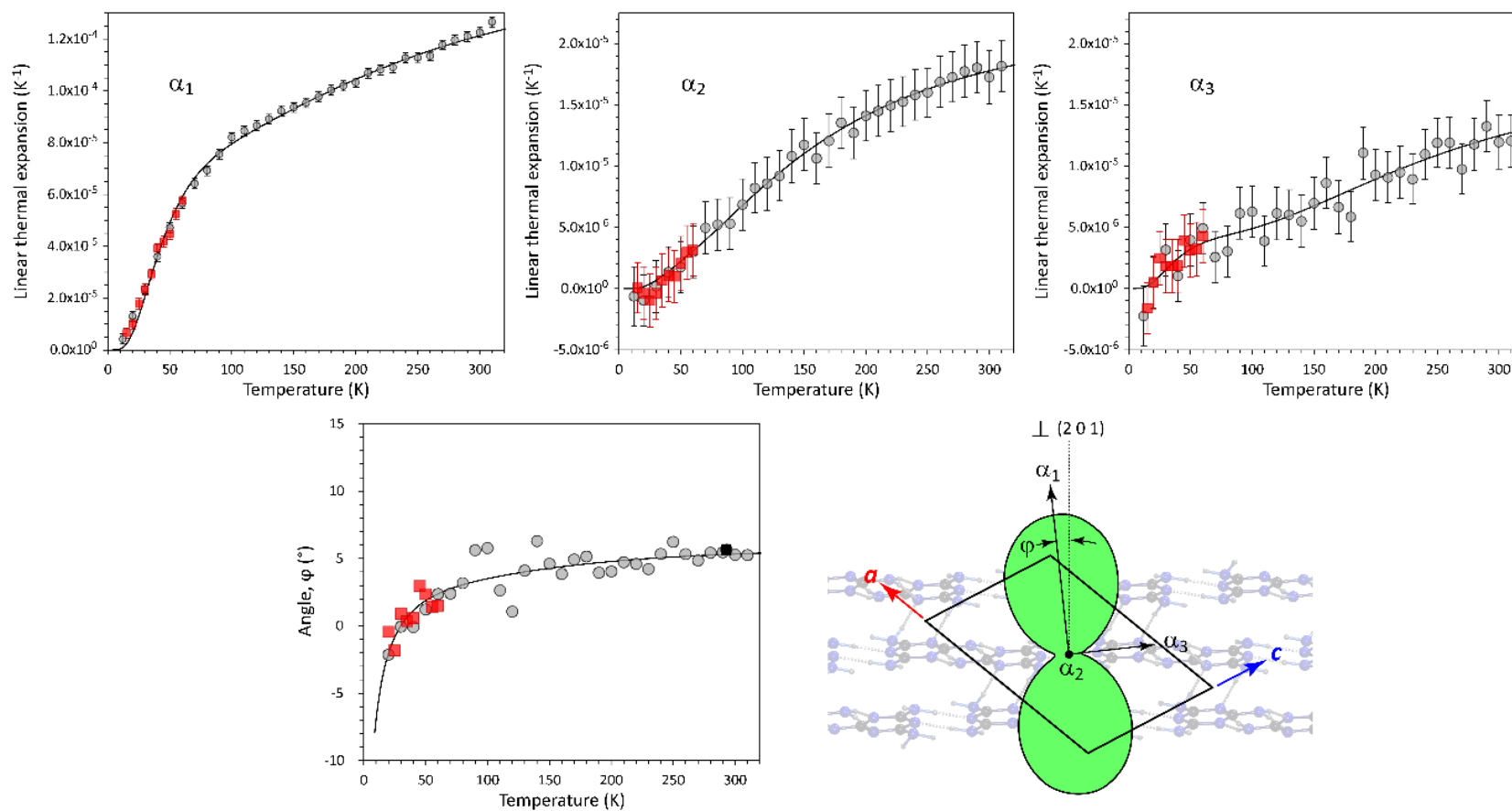
Figure S5

Magnitudes of the principal linear incompressibilities of melamine-d6, plotted in separate scales. At bottom-centre, the angle between the direction of greatest linear incompressibility, K_1, and the sheets of melamine molecules in the crystal is plotted, along with a graphic defining the geometric relationships (bottom right).
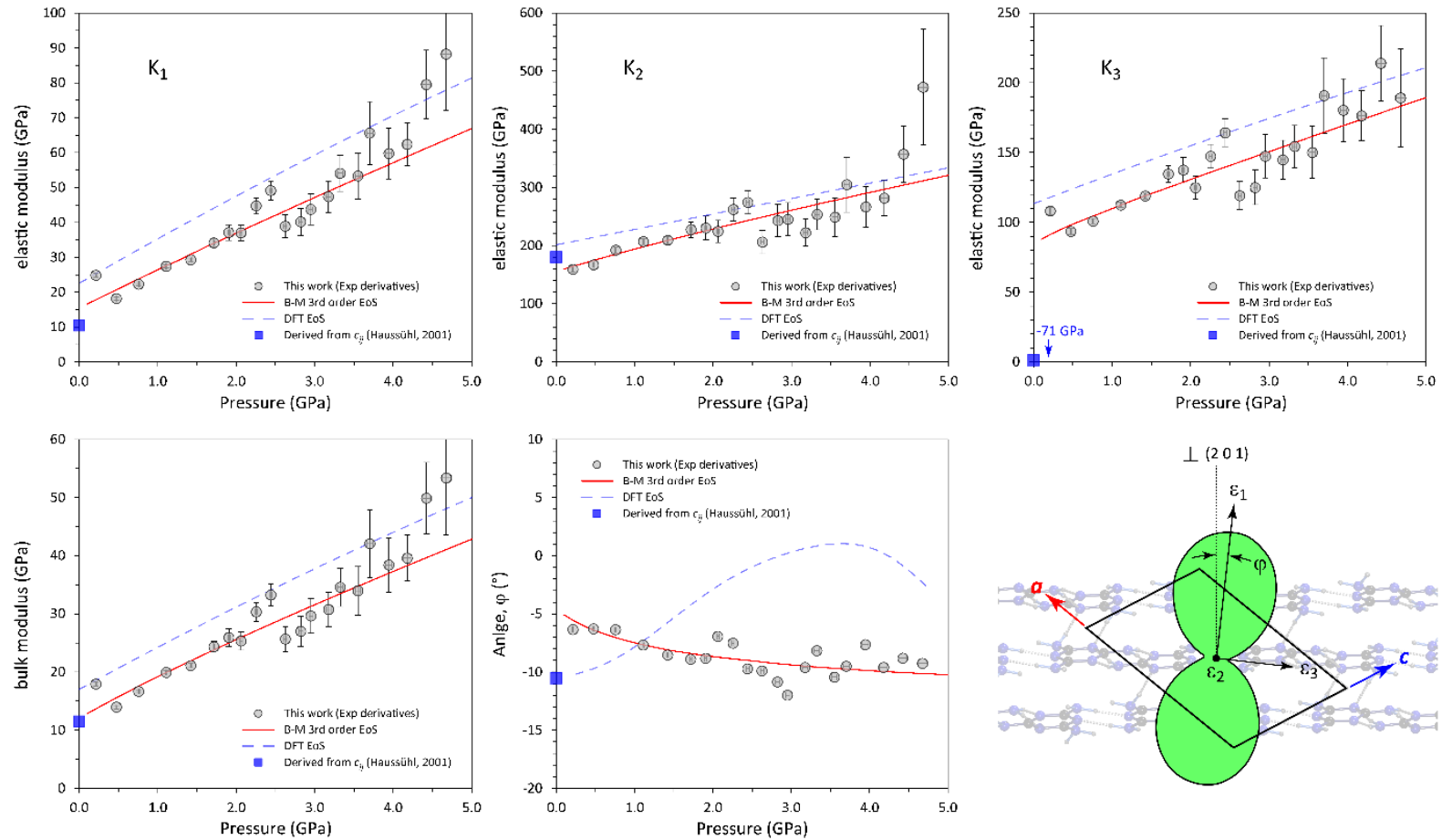
Figure S6

Comparison of our equations of state (experimental and computational) with other literature sources.
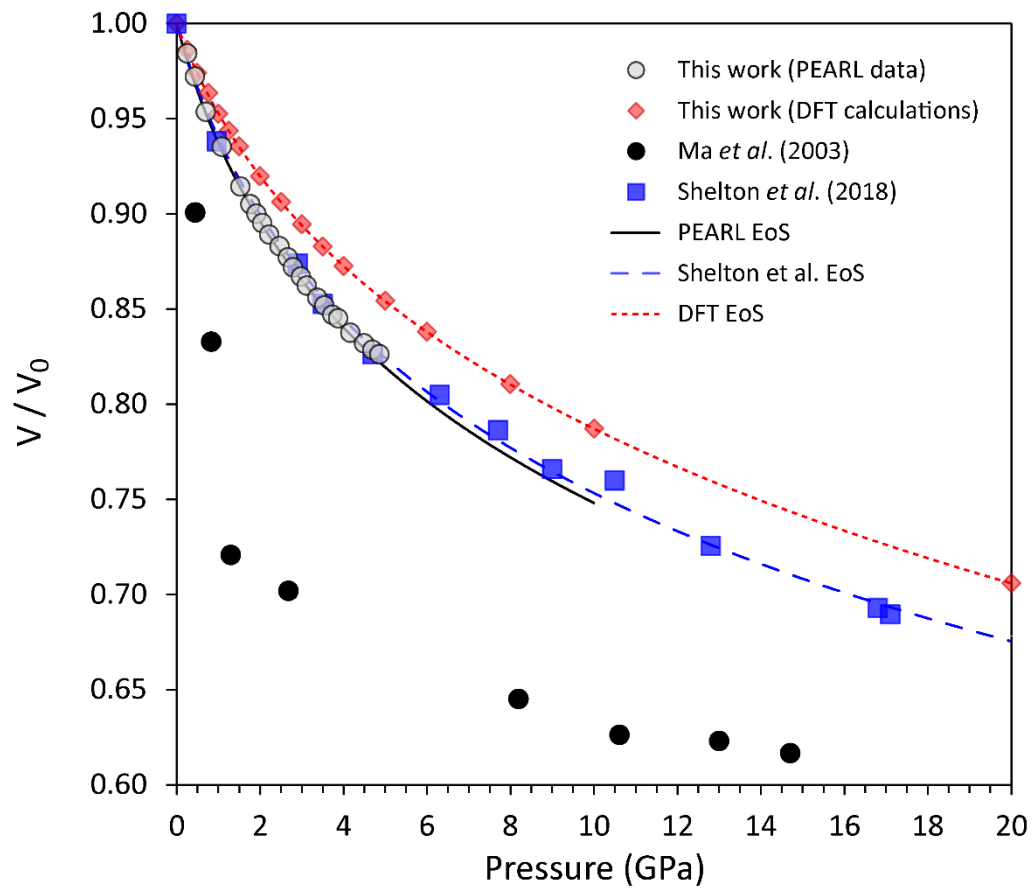
Figure S7

Calculated variation of the C–N bond lengths in the triazine ring of the melamine molecule (left) and between the ring carbons and the amine nitrogens (right). Solid lines are polynomials fitted as a guide to the eye. On the right, filled black symbols report the ambient-pressure 14 K values of Cousson *et al.* (2005); the symbol shapes have the same meaning as the figure legend.
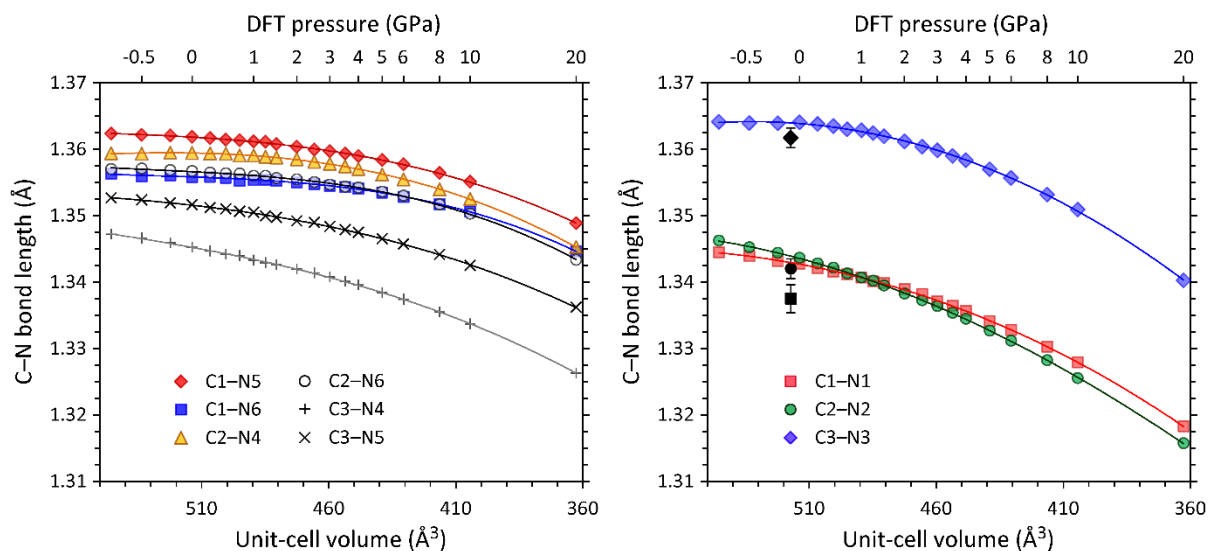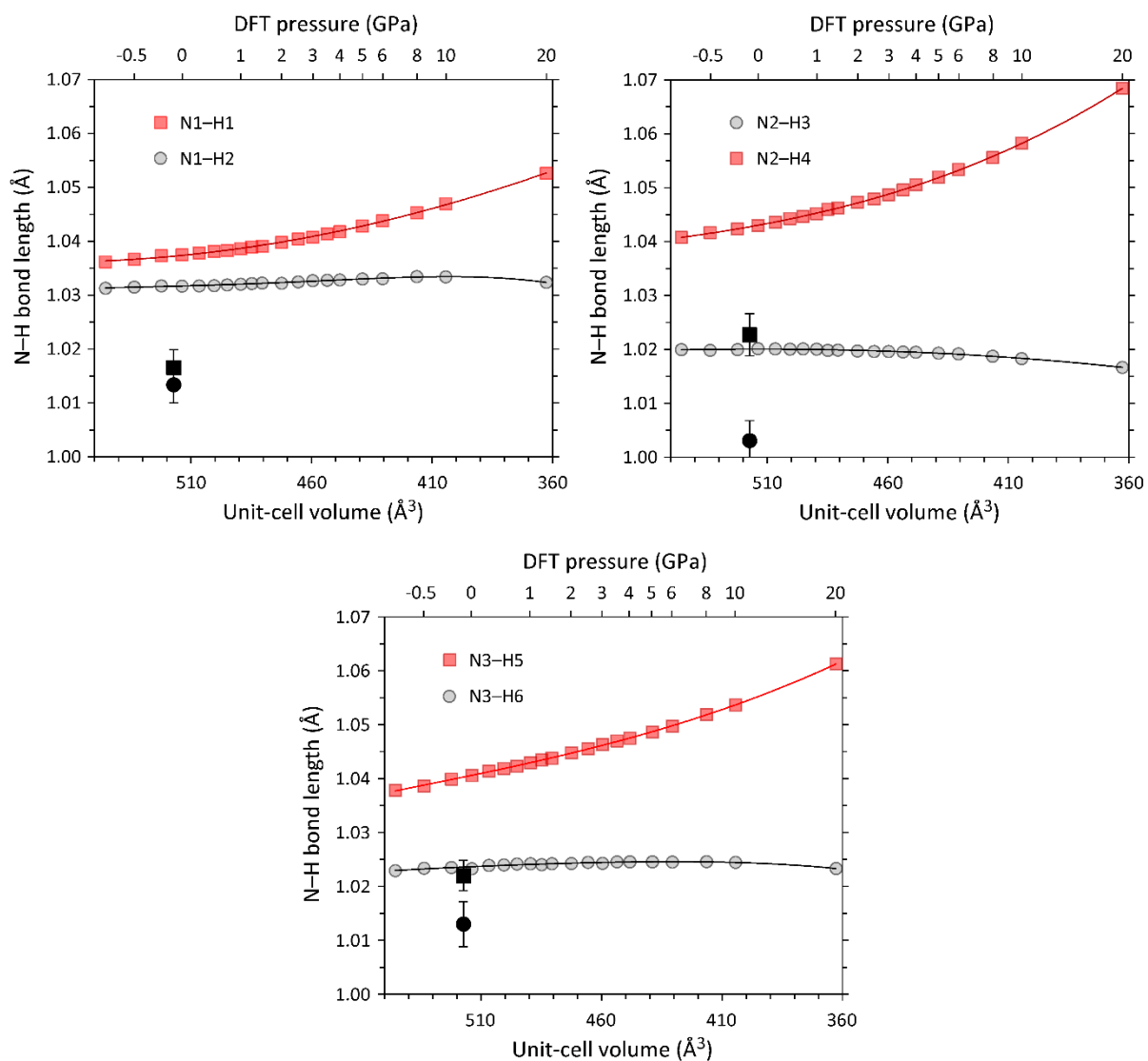
Figure S8

Calculated variation of the N–H bond lengths in each of the three amine groups of the melamine molecule. Solid lines are polynomials fitted as a guide to the eye. Filled black symbols report the ambient-pressure 14 K values of Cousson *et al.* (2005); the symbol shapes have the same meaning as the figure legends.

Fitting of a Debye-type model to the volume thermal expansion

It was determined that a Debye model with only a single characteristic cut-off in the vibrational density of states (VDOS) gave a poor description of the thermal expansion, so additional terms were added such that the temperature dependence of the molar volume could be described accurately as

$$V = V_0 \left[1 + \frac{f(\theta_{D1})}{X} + \frac{f(\theta_{D2})}{Y} + \frac{f(\theta_{D3})}{Z} \right] \tag{S1}$$

where V_0 is the molar volume at zero temperature, the Debye functions, $f(\theta_{D1})$, $f(\theta_{D2})$ and $f(\theta_{D3})$, represent different components of the crystal's internal energy and X, Y and Z are 'mixing parameters'. When the volume is described in terms of single Debye temperature in a first-order expansion of the internal energy the term X, for example, would be $V_0 K_0/\gamma$, where V_0 and K_0 are the zero-temperature molar volume and bulk modulus and γ is a Grüneisen parameter. For the three-term model given above it is sufficient to observe that $X \propto \gamma_x^{-1}$, where γ_x is a Grüneisen parameter corresponding with the vibrational modes described by $f(\theta_{D1})$.

The Debye function is defined as (Cochran, 1973)

$$f(\theta_D) = 9Nk_BT \left(\frac{T}{\theta_D} \right)^3 \int_0^{\theta_D/T} \frac{x^3}{e^x - 1} dx \tag{S2}$$

where N is the number of atoms per molecules, k_B is Boltzmann's constant, T = temperature, and θ_D is a characteristic Debye temperatures, respectively, corresponding to the cut-off frequencies of particular vibrational modes in the VDOS.

Two approaches to fitting Eq. S1 were implemented. In the first, Debye temperatures were obtained from fitting the measured specific heat of protiated melamine (Stephenson & Berets, 1952: Peng et al., 2009), yielding $\theta_{D1} = 166 \pm 5$ K, $\theta_{D2} = 413 \pm 18$ and $\theta_{D3} = 1487 \pm 11$ K; these correspond to cut-off frequencies in the VDOS of 115 ± 4 cm^{-1}, 291 ± 12 cm^{-1} and 1034 ± 7 cm^{-1} respectively. Although the vibrational spectrum measured at 20 K by inelastic neutron spectroscopy (Fernández-Liencres et al., 2001) is more structured, one can discern groups of modes that correspond roughly with the cut-offs determined from the fitting

of the heat capacity. Note that the lower-frequency portion of the data is not shown in the paper by Fernández-Liencres *et al*., but may be found under the entry for melamine in the ISIS INS database (http://wwwisis2.isis.rl.ac.uk/INSdatabase).

Fitting Eq. S1 to the molar volumes determined using our HRPD data, keeping the three Debye temperatures fixed at the values obtained from the heat capacity fit, resulted in a poor agreement between the model and the experimental values. This nature of the misfit indicated that the frequency spectrum of the deuterated solid must differ significantly from that of the protiated material from which the Debye temperatures were derived. This is not surprising since deuteration makes a large difference to the mass and moment-of-inertia ratio of the two isotopologues.

Thus the second approach to fitting Eq. S1 was predicated on an unbiased fit of the Debye temperatures, starting from a single Debye function and adding more terms as necessary. It was found that a very good fit to the experimental data could be obtained with two Debye functions, with no features evident in the residuals motivating the addition of further terms. The parameter values from this 'double-Debye' model fit are, $V_0 = 77.977(1)$ cm^3 mol^{-1} = 517.94(2) Å^3, $\theta_{D1} = 200(3)$ K, $X = 352(5)\times10^4$ J mol^{-1}, $\theta_{D2} = 1179(48)$ K, $Y = 366(12) \times10^4$ J mol^{-1}. Clearly the second Debye temperature represents an average of the two higher-frequency terms reflected in the fit to the heat capacity; attempting to extract further detail concerning the internal energy / vibrational spectrum of the crystal in this way is an exercise in over-interpretation. Experimental measurement of the specific heat and inelastic neutron spectrum of deuterated melamine would be a useful precursor to future analysis.

Cochran, W. (1973). *The Dynamics of Atoms in Crystals.* Arnold, London.

Fernández-Liencres, M.P., Navarro, A., López-González, J.J., Fernández-Gómez, M., Tomkinson, J., Kearley, G.J. (2001). Measurement and ab initio modelling of the inelastic neutron scattering of solid melamine. Evidence for anisotropy in the external modes spectrum. *Chem. Phys.,* **266**, 1–17.

Peng, L., Wei, X., Shan-Zhou, H., Xi, L., Zhi-Cheng, T. (2009). Enthalpy of formation, heat capacity and entropy of melamine. *Acta Phys. Chim. Sin*. **25**, 2417–2421.

Stephenson, C.C., & Berets, D.J. (1952). The heat capacities and entropies of melamine and dicyanamide. *J. Am. Chem. Soc*., **74**, 882–883.

Note about computer graphics

A range of scientific and artistic visualisation computer-software packages were used both to obtain and report data contained in this paper:

Bond lengths and angles, and angles between planes, as well drawings of the molecular architecture of the melamine crystal were produced with *Diamond* (Putz & Brandenburg, 2006) and *Vesta* (Momma & Izumi, 2008, 2011)

Putz, H., & Brandenburg, K. (2006). *Diamond - Crystal and Molecular Structure Visualization*. Crystal Impact - GbR, Kreuzherrenstr. 102, 53227 Bonn, Germany. (www.crystalimpact.com/diamond)

Momma, K., & Izumi, F. (2008). VESTA: a three-dimensional visualization system for electronic and structural analysis. *J. Appl. Cryst.*, **41**, 653–658.

Momma, K., & Izumi, F. (2011). VESTA 3 for three-dimensional visualization of crystal, volumetric and morphology data. *J. Appl. Cryst.*, **44**, 1272–1276. (http://jp-minerals.org/vesta/en/)

Representations of the elastic strain (*cf*., Hashash *et al*., 2003) were generated using *WinTensor* (Kaminski, 2004). These figures were transformed from .wrl to .ply format using Patrick Min's *Meshconv* utility and further transformed into .3DS format with *MeshLab* (Cignoni *et al*., 2008). The representation surface was then imported into *Sketchup* and combined precisely with various geometric markers before being used to generate a high-quality graphic using the bi-directional Metropolis Light Transport algorithm in *Twilight Render*.

Hashash, Y.M., Yao, J.I.C., & Wotring, D.C. (2003). Glyph and hyperstreamline representation of stress and strain tensors and material constitutive response. *Int. J. Num. Anal. Methods Geomech.,* **27**, 603–626.

Kaminski W (2004) *WinTensor* 1.1 (cad4.cpac.washington.edu/WinTensorhome/WinTensor.htm)

Min, P. (1997 – 2017). Meshconv (https://www.patrickmin.com/meshconv/)

Cignoni, P., Callieri, M., Corsini, M., Dellepiane, M., Ganovelli, F., & Ranzuglia, G. (2008). MeshLab: an Open-Source Mesh Processing Tool. *Sixth Eurographics Italian Chapter Conference*, page 129-136. (http://vcg.isti.cnr.it/Publications/2008/CCCDGR08/MeshLabEGIT.final.pdf)

Google Sketchup (https://www.sketchup.com/)

Twilight Render (https://www.twilightrender.com/)